Travelling-Wave Modeling of Dynamics of Ultrafast Reflective-Intracavity-Filter Tunable Fabry-Pérot Lasers for Optical Coherent Tomography

Lixiong Zhang

MSc by research

University of York

Department of Electronics

November 2011

Abstract

The dynamics of Fabry-Pérot external-cavity laser diodes frequency-swept at a high rate using a tunable intracavity filter are investigated by travelling-wave modelling. The effect of broad and narrow bandwidth filter properties and linewidth enhancement factor of the laser performance is assessed in this project. The phenomenon of self mode locking in a laser with a broad filter is discovered and analysed.

List of Contents

List of figures

Acknowledgements

This thesis could not be finished without the help and support of many people who are gratefully acknowledged here.

First and foremost I want to express my deepest gratitude to my dedicated supervisor, Dr Eugene Avrutin, I will not be able to work out this thesis without his guidance. He has offered me valuable ideas and suggestions with his rich research experience and knowledge. His patience and kindness throughout my research period are greatly appreciated.

I would also like to show my gratitude to my dear friends Li Li, Xuetao Yuan, Guan Yang, Zhangxu Wang and Yubo Wang who gave me great encouragements while I was studying and living in and off campus. I must thank my family for their support all the way from the very beginning of my undergraduate study till I finished postgraduate degree.

Declaration

I hereby declare that this thesis is my original research work. All the sources used in this thesis have been clearly referenced. This thesis has not been submitted previously for a degree at any higher institution.

Lixiong Zhang

1 Introduction and background

1.1 Introduction to OCT

Optical Coherent Tomography (OCT) is a high resolution imaging tool which is capable of presenting cross sectional and three dimensional images [1]. It generates those images by analysing the time delay of reflections of penetrating light.

3-D OCT imaging technique is now widely used in medical practice, but the need to improve the resolution, penetration depth, and information acquisition rate means that it continues to be studied by a number of researchers. [2-6]

OCT has been increasingly used in a variety of applications such as ophthalmology, cardiology and dentistry [8], as well as in breast cancer detection. [11] The OCT technique is based on shining near infrared light on semi-transparent object such as tissues. Although the biological tissue have light scattering properties which limits light penetration through the body tissue to 2 mm, this imaging depth is enough to provide valuable information about tissue structures. [7]

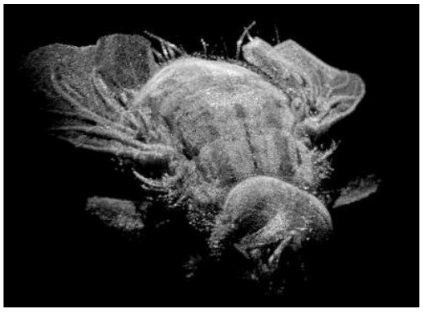

Figure 1a OCT image of a house fly [9]

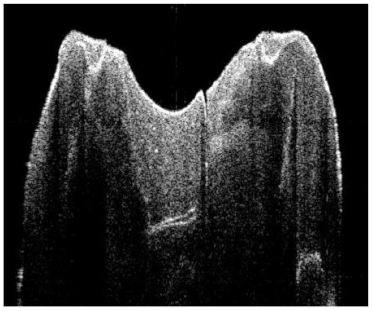

Figure 1b OCT image cross section of a tooth[9]

Figure 1a shows an OCT image of a house fly and Figure 1b shows image of a tooth, both of them are measured at the wavelength 1300 nm by using rapidly tuned Fabry-Pérot lasers (RFPTL) [9]

Optical Coherence Tomography analyses interferences between light reflected from tissue and a reference reflector can be achieved by means of either time domain or frequency domain techniques.

There are two main OCT approaches: Time domain and Frequency domain.

Time-domain OCT is the simplest method of OCT technique. It uses broadband light source injected into an interferometer which includes a translating reference mirror. [12] The time delay is mechanically scanned. Unfortunately, the method is slow and has poor sensitivity.

Frequency-domain OCT (FD-OCT) has advantages over the *time-domain* OCT (TD-OCT). The data acquisition time in FD-OCT is much faster than that in Time- domain as there is no mechanical scanning over the biological tissue. Signal-to-noise ratio (SNR) is improved considerably in FD-OCT [14]–[19]. The basic Spectral or *Frequency-domain* OCT includes interferometer, spectrometer, diffraction grating and detector array.

Frequency-domain OCT techniques, in their turn, fall into two categories: *Swept-source OCT* and *Fourier-domain* OCT.

Fourier-domain OCT utilises a diffraction grating and charge coupled device array to obtain the spectral interference pattern in the spectral domain. The depth structure is obtained almost at one time and the depth scan is not needed. The acquisition time is fast and is only limited by the readout speed of the charge coupled device which records the scattered light intensity in frequency not time. [13]

The *swept-source OCT* (SS-OCT) technique is another form of Frequency-domain OCT which has drawn a lot of attention recently from both researchers and practitioners. SS-OCT has a frequency-sweeping source and a single photo detector which detects the wavelength-resolved interference signal. In addition to the common advantages of the Frequency-domain method over *Time-domain* OCT, *swept-source* OCT has some advantages over the *Fourier-domain* OCT, namely faster data acquisition, smaller and simpler system is practical as light is directly coupled to detector without dispersion by grating. [19]

It is this technique that is the subject of this thesis.

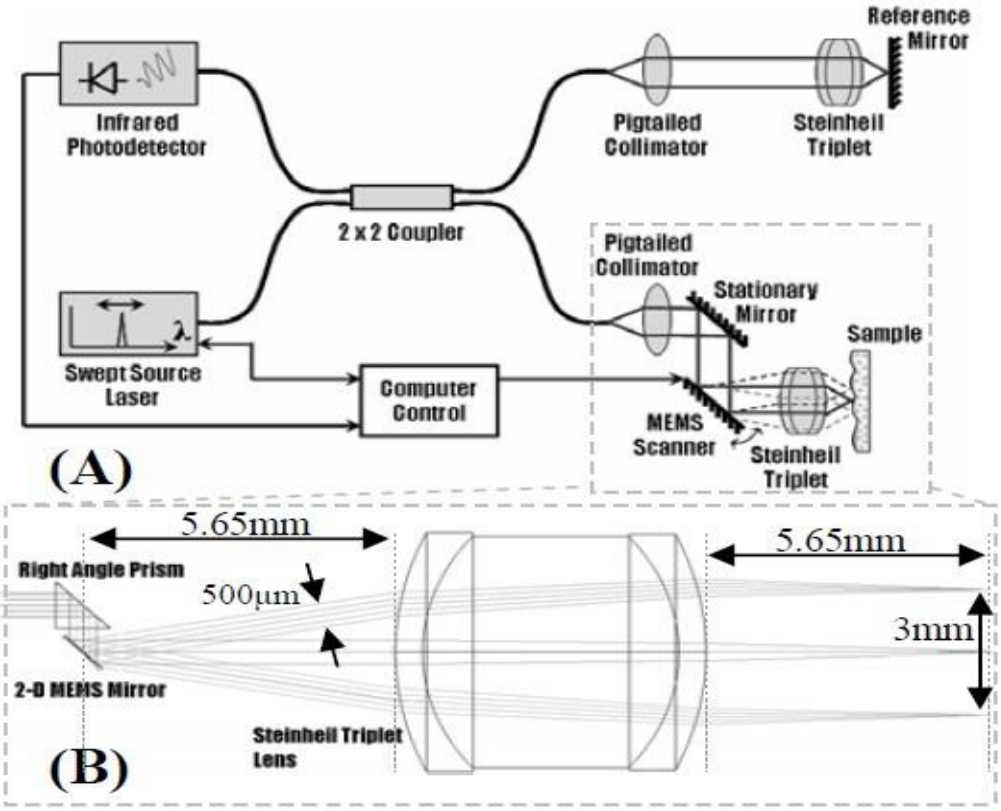

Figure 2 An example setup of forward-imaging SS-OCT system (A) with Optical characteristics of scanning system (B) [25]

Figure 2 shows the setup [25] of forward-imaging SS-OCT system. Key to the success of the technique is the swept-source laser, which is the specific subject of the thesis.

SS-OCT has a number of advantages. For instance, it can be realised inexpensively at wavelengths of 1060nm and 1300 nm where tissues are transparent. Fourier-domain OCT is difficult at these wavelengths because the photodetector arrays that it requires are either very expensive or not available at all.

However to realise the advantages of this technique, one needs a laser with a good performance. A good laser performance, in turn, can be defined by a number of aspects:

Firstly, broad tuning range is required for good resolution, typically greater than 100 nm tuning range for imaging resolution of < 15 μm.

Secondly, a coherence length longer than 10mm is needed, to achieve the OCT imaging depth of greater than 5mm. The long coherence length L_c corresponds to a narrow dynamic laser linewidth $\Delta\lambda$, due to the well-known relation

$$L_c = \frac{c}{\Delta\lambda}$$

c being the speed of light. A value of 13.2 GHz (or <0.074 nm) has been quoted in literature [9].

Thirdly, fast scan rates are required for fast data acquisition. Typically, 20 – 100 kHz scan rates are required. From the tuning range and scan period,

we can estimate that the tuning speed should be up to a few GHz/ns, as illustrated schematically in Figure 3.

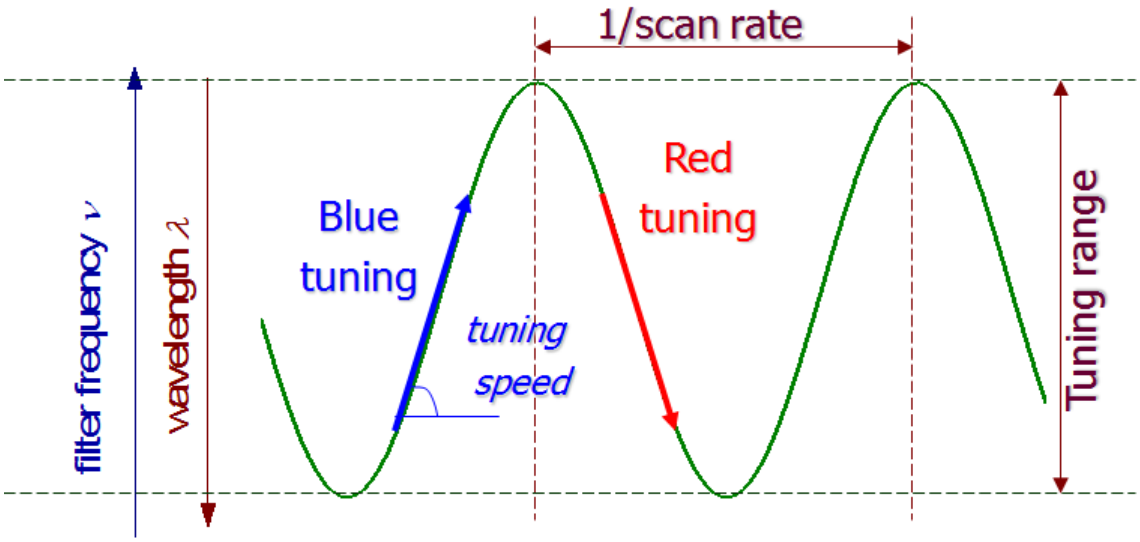

Figure 3 Schematic of the frequency scanning, illustrating the relation between the scanning rate, tuning range, and tuning speed.

The two peaks from horizontal direction represent the scanning period T_{scan}, which is the inverse of the scan rate. The vertical axis is filter frequency or wavelength, from top to bottom represent the tuning range $\Delta\nu_{tuning}$ of the source (which is typically given by the tuning range of a tunable filter that the source uses). Then, the maximum tuning speed needed during each scan is estimated as

$$\frac{d\nu_f}{dt} \approx 2\frac{\Delta\nu_{tuning}}{T_{scan}}$$

If the tuning range is approximately 100 nm, central wavelength $\lambda \approx 1.06$ μm and scan rate is from 20 to 100 kHz, this means the tuning speed required is from $d\,\nu_f/dt \approx$ 1.2 to 6 GHz/ns.

We refer to tuning towards shorter wavelengths/higher frequencies as blue tuning and to tuning towards longer wavelengths/lower frequencies as red

tuning, as illustrated Figure 4 (in the literature, the terms “positive and negative tuning” are sometimes used, but we find them potentially misleading as it is not quite clear whether they refer to frequency or wavelength).

In addition, the laser construction needs to be compact. The reason for that is illustrated by Figure 4 below.

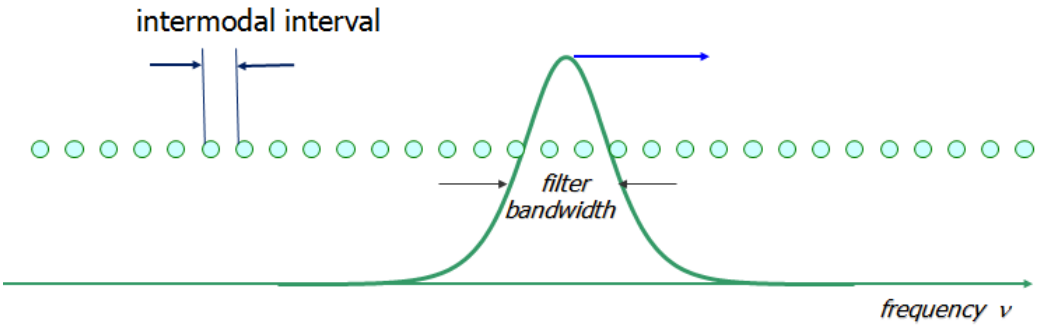

Figure 4 Filter sweeping in modes

The figure above shows a schematic example of how the filter is performing sweeping in a laser.

The space between the two dots represents intermodal interval $\Delta\nu$, and the bell-shaped curve schematically shows the spectral selectivity of a tunable filter. When the filter is sweeping past laser modes, each mode exists in the spectrum for a time interval which can be estimated as the ratio of filter bandwidth to tuning speed.

$$Time\ past\ through\ the\ filter = \frac{filter\ bandwidth}{tuning\ speed}$$

During this time, the mode must build up in the spectrum. Otherwise, no mode will be caught by the filter bandwidth. The formation of the mode itself needs the light to undergo several round-trips within the laser cavity to build

up. For this reason, the round-trip needs to be as short as possible which means the laser cavity needs to be as short as possible. An estimate with the parameters we have is a few centimetres in air and this is the construction that our industrial contacts have developed. This construction will be discussed below.

2 Literature review

2.1 The experimental and modelling work on ring lasers

The previous work on semiconductor lasers for swept-source OCT used a wavelength-swept ring laser. It has been studied for faster image acquisition rates and higher spatial resolution. Generally, it requires fast repetition rates of greater than 15 kHz, broad tuning ranges of longer than 50 nm and narrow instantaneous linewidths of smaller than 0.1 nm. [20]

A theoretical investigation of this construction has also been conducted [20].

Figure 1 is a schematic of the ring laser model used in [20]. It has a Semiconductor optical amplifier section to be the gain medium followed by a linearly tuned optical filter, then an output coupler and a fiber cavity. The long cavity length is 7.4 meters.

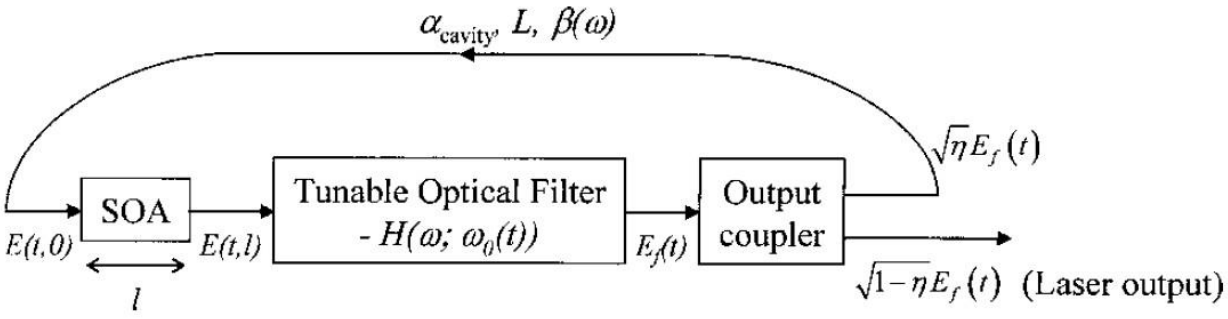

Figure 5 Schematic diagram of the model of a wavelength swept semiconductor ring laser incorporating a tunable intracavity filter. [20]

A noticeable feature that found in a ring laser was that there is a dramatic power loss in negative tuning which was defined as sweeping in the direction of wavelength decreasing (blue tuning, in our notations), and only positive or increasing wavelength tuning (red tuning, in our terms) could be achieved steadily. Therefore, the wavelength tuning is practically limited to positive wavelength tuning which is increasing wavelength tuning. This sort

of asymmetric behaviour was attributed to the four-wave mixing in SOAs as there is a negative frequency shift while the light pass through the SOA and it was reported in [21] previously. [20]

This asymmetric behaviour is an important feature of fast swept lasers and has been investigated in our work as well, as will be reported below.

The numerical method used in [20] was a travelling-wave laser model with a Langevin spontaneous noise source.

$$\frac{\partial g_l(t,z)}{\partial t} = \frac{g_0 - g_l(t,z)}{\tau_s} - \frac{g(t,z)|E(t,z)|^2}{E_{\text{sat}}},$$

$$\frac{\partial E(t,z)}{\partial z} + \frac{1}{v_g}\frac{\partial E(t,z)}{\partial t} = \frac{1}{2}[g(t,z)(1 - i\alpha) - \alpha_{\text{int}}]E(t,z) + n(t,z),$$

g_l being the linear gain, in the terminology of the authors of [20]

g_0 the small-signal gain coefficient determining the unsaturated gain due to pumping

τ_s the carrier lifetime (assumed linear),

E_{sat} the saturation energy,

v_g the group velocity inside the SOA,

α the linewidth enhancement factor,

α_{int} the waveguide losses,

$h\omega_0$ the single photon energy,

and n_{sp} the population inversion factor.

$g=g_l /(1+\varepsilon E/2)$ is the nonlinear gain, where ε is the nonlinear gain suppression parameter.

$N(t, z)$ is a spontaneous-emission noise

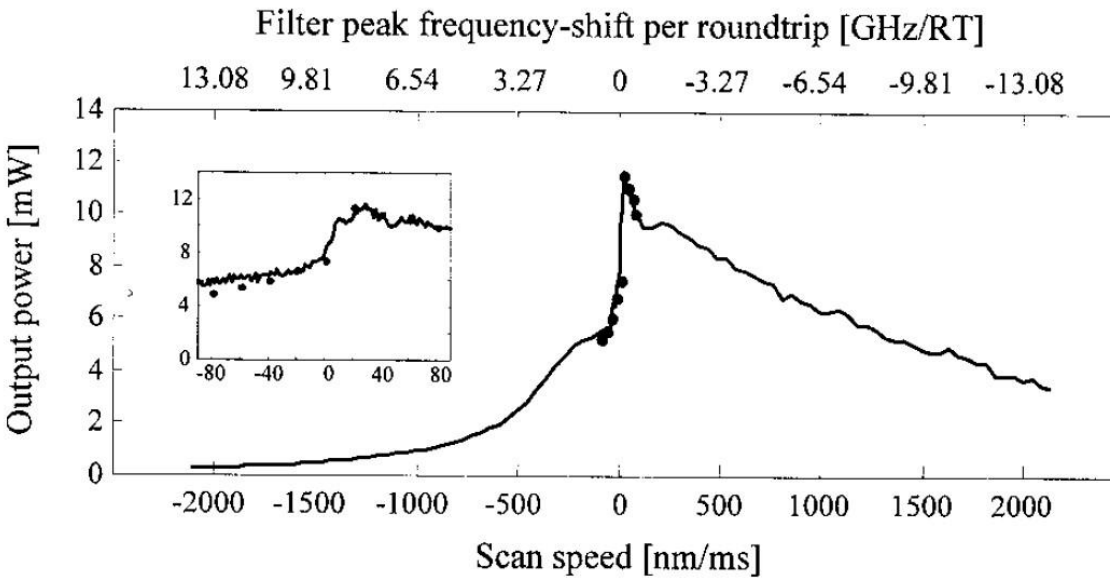

Figure 6 Laser output power versus scanning speed [20]

The main features obtained in this investigation on wavelength-swept SOA ring laser are that lower scanning speed gives the higher output power and the power decays as the scanning speed increasing. However, positive tuning speed is not dropping as fast as the negative ones. It drops to almost zero at -2000nm/ms but remains just under 4mW at same speed of 2000nm/ms.

This asymmetric dropping in power is what we need to investigate in our work, though using a different construction, as discussed below.

2.2. The Fabry-Pérot fast tunable laser construction and measurements

The subject of our modelling is the compact reflective Fabry-Pérot tunable laser (RFPTL) similar to a construction proposed recently by a US firm, Axsun Technologies. This semiconductor laser with external cavity uses a novel, recently developed silicon Micro-Electro-Mechanical System (MEMS) tunable Fabry-Pérot filter which works in a reflective, rather than transmission, operation mode. [8] The structure of the laser is shown schematically in Figure 7.

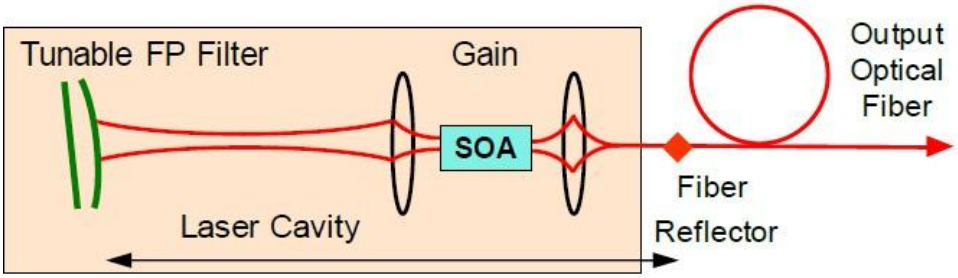

Figure 7 Reflective Fabry-Pérot tunable laser RFPTL configuration. [8]

The reflective Fabry-Pérot tunable laser (RFPTL) construction can have shorter laser cavities or longer laser cavities. With a shorter laser cavities (10 –30 mm), the second cavity mirror is inside the laser package whereas the longer laser cavities (5-100cm and greater), the second cavity mirror is on the fiber outside the laser package. [9]

We simulate a laser cavity about several centimetres long in our model. A too-short laser cavity can only have one single longitudinal mode fit in the filter passband envelope. We want laser can tune both single and multi modes. Generally speaking, it is still a relative short laser cavity compare to the ring laser which has a laser cavity of a few metres longs as described

earlier. So it is a simpler and more compact Fabry-Pérot construction used in our model and in [8].

The most important component device of the RFPTL laser is the silicon MEMS tunable Fabry-Pérot (FP) filter [10], as shown schematically in Figures 8 (general view) ans 9 (structure), reproduced from [8]. The construction of the filter includes a HR coated flat mirror and a HR coated curved mirror on tethered membrane, which is electrostatically actuated. The filter forms one of the two mirros of the Fabry-Pérot cavity. This MEMS filter has scan rates that exceed 100 kHz and its tuning range can range from 40nm to 350nm and can be varied by changing the design. [8]

This means that the filter is capable of very fast tuning speed, up to several GHz/ns

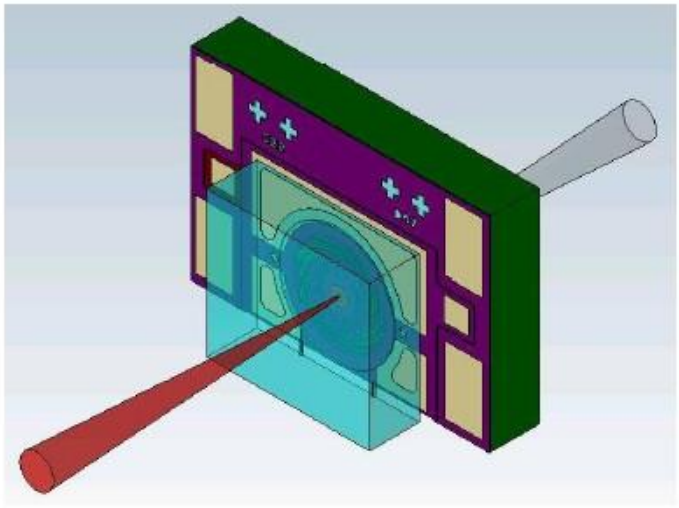

Figure 8 Silicon micro-electro-mechanical system (MEMS) tunable Fabry-Pérot filter. [8]

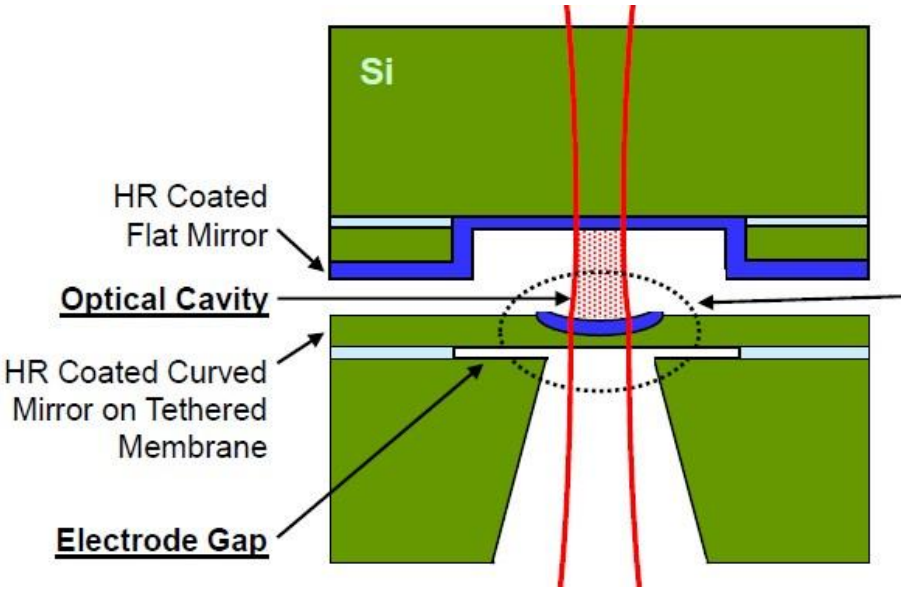

Figure 9 MEMS Fabry-Pérot Filter structure [9]

The performance of Axsun filter is illustrated in Figure 10, reproduced from [10],

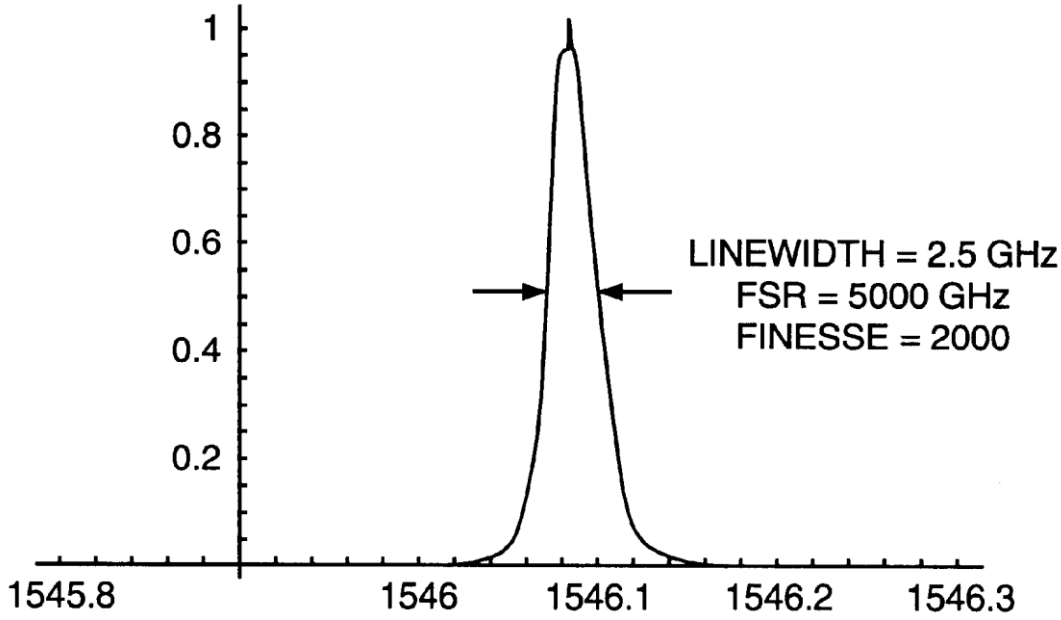

Figure 10 Performance of Axsun Gap + Si F/P Filter [10]

Unlike a plane Fabry-Pérot filter, which has narrow spectral transmittance peaks and broad reflectance maxima, this novel convex Fabry- Pérot MEMS filter has a sharp filter reflectance peak as well as the sharp trasmittance peak. The filter bandwidth can vary from 2 to more than 20 GHz/ns depending on the construction and the voltage on the MEMS filter.

The measured laser performance is illustrated in Figure 11. The optical power vs. wavelength is shown for two scanning speeds.

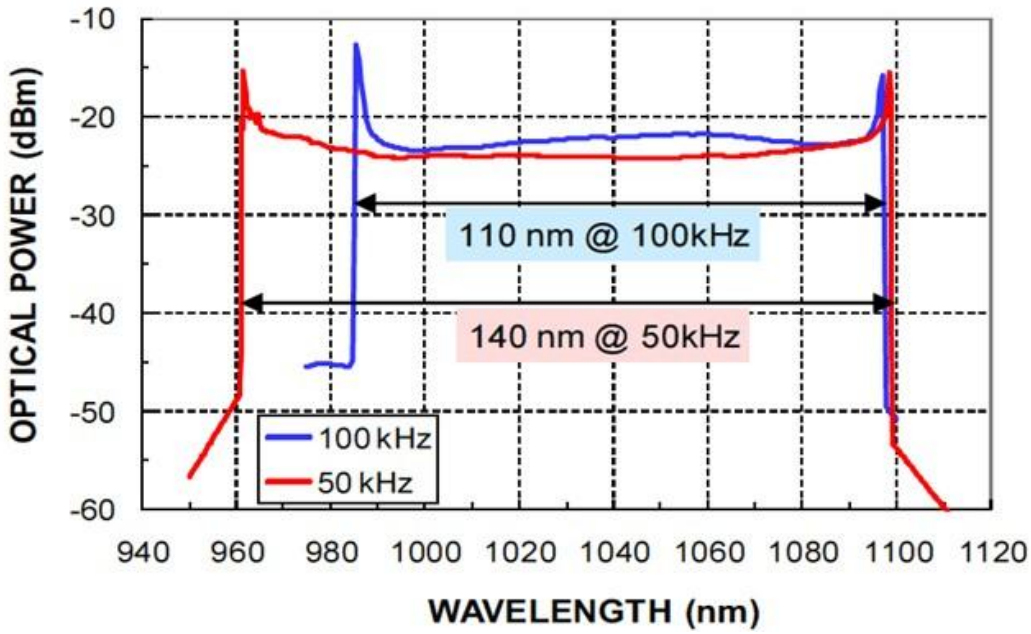

Figure 11 The measured tuning curves of the RFPFL [8]

The above diagram gives a picture of tuning range with complex dependence of power on wavelength, tuning speed.

As can be seen from the figure above, red tuning has a broader tuning range than the blue tuning. In addition, private communications from experimentalists say that the optical power for red tuning is more regular than that of blue.

3 Objectives of study

Based on the overview above, the objectives raised to our modelling are:

- to analyse further the blue-red asymmetry, to find out to what extent the power asymmetry seen in the ring lasers is reproduced in Fabry-Pérot ones
- To analyse the laser dynamic regimes and see why the red tuning is more regular than blue tuning.
- To study the effects of laser and filter parameters on the performance.

4 Developing the model

4.1 Introduction to LasTiDom

The LasTiDom [23] software has been used in simulating passive or active devices such as resonators (passive) and lasers or amplifiers (active) for producing pulsed output. For instance, mode-locked or Q-switched lasers or amplifiers with pulsed input can be used. In this work, we adapt it to simulate lasers with an intracavity filter.

The model is to some extent similar to that used by the previous authors [20], the main differences being that:

- Firstly, bidirectional (forward and reverse) propagation is taken into account as usual for a Fabry-Pérot structure, whereas the model of [20] is for a unidirectional ring laser.
- Secondly, the model is somewhat more realistic, taking into account carrier-dependent recombination rates and gain dispersion.
- Thirdly, the model is entirely time-domain, as will be discussed below.

4.2 The Model as used in this work

The model used in this report is one dimensional. Only the propagation in the longitudinal direction is studied in detail; it is assumed that the laser waveguide is strong enough that any variations of carrier density and light distribution in the lateral and transverse directions have only minor effects on the laser performance. The cavity length which consists of gain and passive sections can be from 1 to 10 cm adjustable.

The filter is assumed to act as the reflecting mirror on one end; the filter model will be considered in more detail below.

The gain section is assumed to be a Multi-Quantum Well (MQW) semiconductor laser amplifier with typical parameters taken from literature. It is well known that an MQW gives a better optical performance and compact laser design over many conventional laser diodes [24]. Therefore, we used logarithmic gain-carrier density dependence, typical in modelling quantum well lasers, and a relatively small value of the linewidth enhancement factor (α_H= 2) which is typical for quantum well materials.

The laser has two mirror effect surfaces that situated at both end of the laser cavity. External cavity laser diode is used in the model. The light travels inside the laser in forward and reverse direction due to the reflecting surface and forms the optical waveguiding in the laser cavity. See figure below. A mode is formed during the time light travels back and forth within the laser cavity. The mode needs a few roundtrips to build up, but each mode only lases for a few roundtrips.

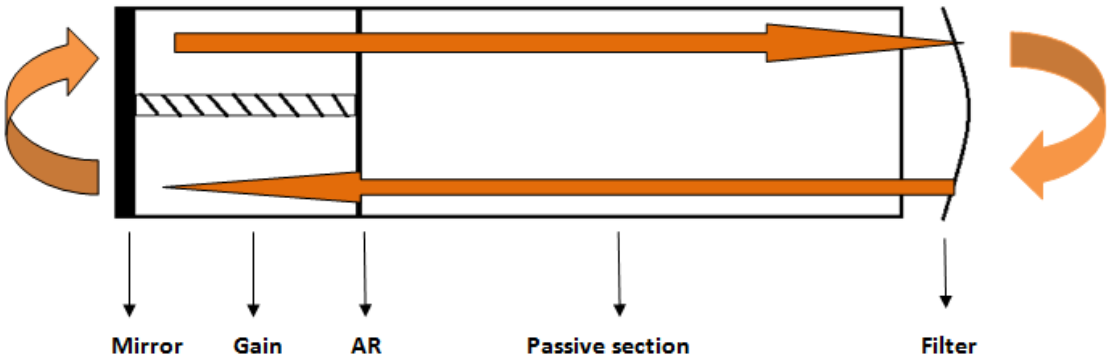

Figure 12 Schematic of Lorentzian laser diode with gain and passive section.

We use a travelling wave model, which includes Light propagation, Gain, with parabolic dispersion. Self-phase modulation and spontaneous noise to start the model.

The model of the laser, in its main features, is not new. It has been used for many laser constructions before (see for example [23] as an overview). The new part is the filter, as discussed below.

For the gain-current density relation, we follow [27] in using a two-parameter logarithmic fit

$$g(N,S) = \frac{G_0}{1+\varepsilon S} \ln \frac{N}{N_0} , \tag{1}$$

(where N_0 and G_0 are the transparency carrier density and gain constant respectively, and ε the gain compression factor) for both QW and bulk active layers, with parameters taken from [27].

We use a travelling–wave model LasTiDom [27，28] which includes one-dimensional propagation, along the longitudinal coordinate z, of slow amplitudes ER,L of right- (forward) and left- (reverse) travelling light :

$$\mp \frac{\partial E_{L,R}}{\partial z} + \frac{1}{v_g} \frac{\partial E_{L,R}}{\partial t} = \frac{v_g}{2} \left((\Gamma \hat{g} - a_i) E_{L,R} + i\Gamma\alpha (g - g_{th}) E_{L,R} \right) + F_{spont}(z,t) \tag{2}$$

Here, g and α_i stand for the optical gain and the internal dissipative loss，α is the Henry linewidth enhancement factor, g_{th} is the threshold gain, and F_{spont} is the Langevin spontaneous (random) source that ensures self-starting of the model and introduces noise. The operator nature of $\hat{g}$ represents gain dispersion; in the model version that we used, the operator simulates a Lorentzian curve using an integral relation,

$$\hat{g}\,E_{R,L} = g(N,S)\Delta\Omega' \int_{o}^{\infty} E_{R,L}(z,t-\tau)\exp(-\Delta\Omega\tau)d\tau \tag{3}$$

---

with $\Delta\Omega=\Delta\Omega'+j\Delta\Omega''$ being the complex gain curve parameter whose real and imaginary part represent the gain curve width and position respectively (the latter is taken as $\Delta\Omega''= \Delta\Omega''_N(N-N_{th})$ to model the shift of the gain peak with carrier density). Furthermore, $g(N,S)$ is the peak gain value, determined by the local carrier density N(z,t) and photon density

$$S(z,t) = E_R^2(z,t) + E_L^2(z,t)$$

At the laser facets standard reflection/ transmission boundary conditions are imposed on ER,L.

The field propagation equations are coupled with co-ordinate-dependent rate equations for the carrier density:

$$\frac{d}{dt}N(z,t) = \frac{J(z,t)}{ed} - N\left(\frac{BN}{1+B_2N} + \frac{1}{\tau_{nr}} + CN^2\right) - v_g \,\mathrm{Re}\left(E_L^{*}\,\hat{g}\,E_L + E_R^{*}\,\hat{g}\,E_R\right) \tag{4}$$

Here, J/ed is the pumping term, with J the current density (with homogeneous pumping, $J=i/WL_{act}$, i being the current and w and L_{act}, the stripe width and length; carrier capture dynamics can be taken into account

in the model, but we verified that it is not too important for the relatively long pulses generated), e the elementary charge, d the active layer thickness, τ_{nr} the non-radiative recombination time, and C the Auger recombination coefficient (both negligible as we consider a GaAs/AlGaAs structure). The last term is the stimulated recombination, with the slow wave amplitudes $E_{L,R}$ measured in units of square root of photon density. The output power is calculated inform the photon density at the output facet:

$$P(t) = \hbar\omega\, v_g \frac{dw}{\Gamma_a}(1-R_L)\left|E_L(0,t)\right|^2$$

where the left (output) facet (with an intensity reflectance R_L) is assumed to be at z=0.

4.3 Including the filter in the model

The new feature that had to be added to LasTiDom for the purpose of this research is a model of the tunable Fabry-Pérot filter. Since the convex filter is a substantially two-dimensional structure, we could not model it from first principles in our one-dimensional model.

The measured performance of the Axsun filter can be approximated by either a Lorentzian (in blue dashed lines) or Gaussian curve (in red dashed lines). They have the same shape around the top but different FWHM can be noticed. In [20], the Gaussian filter was used, so the authors had to simulate the light propagation in time domain and the filter of their ring construction in frequency domain.

As regards the construction we are simulating, it can be seen that neither the Lorentzian curve nor the Gaussian curve fit the spectral response of the Axsun filter exactly, but we choose Lorentzian filter approximation which

with only a small inaccuracy compared to the measured filter reflectance [22] and it can be implemented in the digital filter more easily as was done in [23]. This helps keep our modelling is fully in time domain.

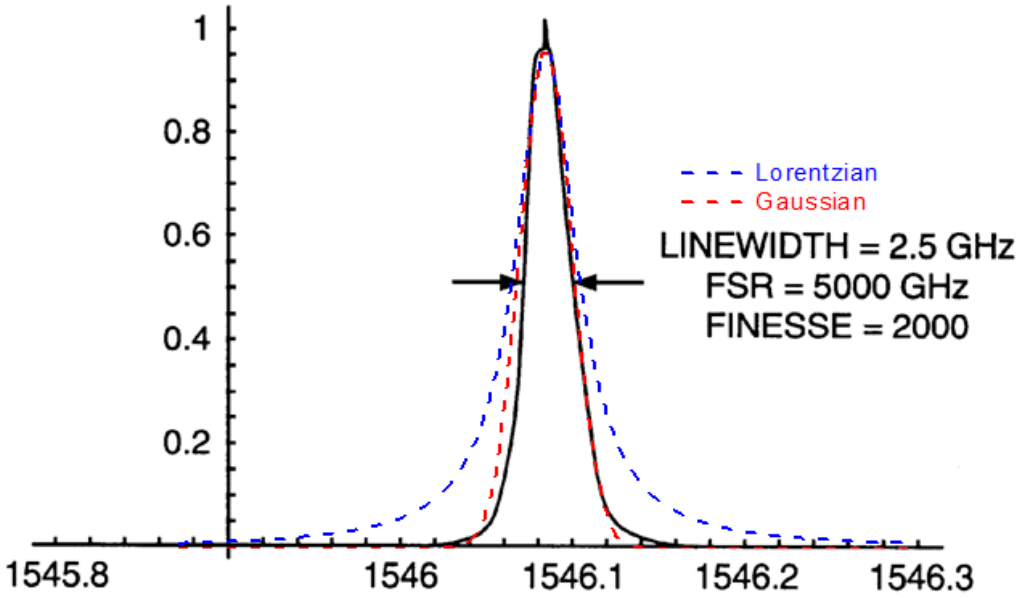

Figure 13 Comparisons of measured filter reflectance curve [22] to Lorentzian and Gaussian filter approximations. *Measured data from: D. C. Flanders, W. A. Atia, B. C. Johnson, M. E. Kuznetsov, C. R. Melendez, "Optical coherence tomography laser with integrated clock, "US Patent Application 2009/0290167 A1*

As we can see from the graph, the Lorentzian approximation for the filter is reasonably accurate and presents good approximation to the measured filter reflectance curve, particularly near the top, which is the important bit in practice. It can be easily implemented in time domain as a convolution similar to those used for gain spectrum. In frequency domain, the (complex) Lorentzian reflectance spectrum is written as

$$\hat{E}_r = \hat{\rho}\,\hat{E}_f = \frac{\rho_{\max}}{1 + j\,\dfrac{\Delta\omega - \Delta\Omega_{filter}(t)}{\delta\Omega_{filter}}}\,\hat{E}_f \tag{5}$$

which in time domain corresponds to

$$E_r = \hat{\rho} E_f = \rho_{\max} \delta\Omega_f \int_o^{\infty} E_f(t-\tau) \exp\left[\left(-\delta\Omega_f + j\Delta\Omega_f(t-\tau)\right)\tau\right] d\tau \quad (6)$$

The filter bandwidth is $\delta\Omega_{filter} = 2\pi\delta\nu_{filter}$, and the swept peak frequency detuning is $\Delta\Omega_{filter}(t) = 2\pi\Delta\nu_{filter}(t)$

We focused on geometries with gain section of a length L_{act}≈ 500 μm and passive section of an equivalent length in a semiconductor of 15000 μm, or 1.5 cm (in air, the length needs to be multiplied by the refractive index of the semiconductor). The construction is an external resonator one, with the filter placed at the end of the laser construction, the filter is separated from the active section by the passive section.

We assumed the refractive index is of 3.5, the round-trip period can be calculated using the usual formula

$$T_{rt} = \frac{2L}{v_g} = \frac{2n_g L}{c}$$

where *L* is the total length of the cavity, including both the gain section and the passive section, *n* is the refractive index in the semiconductor material, therefore *nL* is the total length in air (as usual, in travelling wave models there is no difference between phase and group refractive index), $\mathbf{V_g}$ is the group velocity, c=3.10^8 m/s is the speed of light.

In our construction, the length is L=500 μm+15000μm, the refractive index (phase and group) is n=3.5,

Hence we have

$$T_{rt} = \frac{2n_g L}{c} = \frac{2 \times 3.5 \times 15500 \times 10^{-6}}{3 \times 10^{-8}} \text{ s } \approx \text{ 362 ps}$$

The intermodal interval is then $\Delta\nu_{\text{mod}} = 1/T_{rt} \approx$ 2.77 GHz.

5 Simulation results

5.1 General features.

We knew from our contacts in industry that there were two types of laser resonator corresponding to different dynamics: a short resonator and a long resonator. The short resonator corresponded to the case of the filter bandwidth being comparable or smaller than, the intermodal interval; and the long resonator, to the case of the filter bandwidth significantly greater than the intermodal interval. Rather than change the resonator length, we initially implemented these different situations by changing mainly the filter bandwidth. We started with analysing the case of a narrow filter bandwidth; the chosen value of 2GHz is smaller than the intermodal interval of 2.7GHz interval, but of the same order. Then, we analysed a filter with a broader bandwidth of 20 GHz.

Under tuning, the filter central frequency is fast changed. In a real experimental situation, the frequency tuning is in the form of *scanning*, which means that the filter central frequency is changed sinusoidally at a speed much slower than the typical time scales of laser dynamics (at a frequency of 50-100 kHz, as shown in Figure 3. This takes too long to simulate; therefore, following the work by the previous researchers [20] we model, not the periodic scanning, but sweeping of filter frequency with a given constant speed: $d\nu_{filter}/dt$ =const. This is actually close to what happens during more than half of the scanning period, when filter tuning speed $d\nu_{filter}/dt$ is approximately constant (Figure 3).

5.2 Dynamics of a laser with a narrowband filter

The programme is set to start registration at 10 ns and the filter tuning is set to start after 20 ns; therefore, before the time 20 ns, laser gives a constant CW output power.

In this steady state, the filter is tuned to one of the cavity modes, this mode is taken as the reference frequency of the model and its spectral location is exactly at the peak of the gain spectrum. For definiteness, we number it mode 0; in this case,

ν_0-ν_{ref} =0,

where ν is optical frequency and ν_{ref} is reference frequency of the model

From 20 ns onwards, the filter starts to tune the laser. Initially, this leads to the output power dropping dramatically to nothing (from 20 to 35 ns) as the original laser mode (mode 0) is no more within the filter band and the new modes have not yet formed.

The subsequent intensity dynamics is discussed below.

5.2.1 Intensity dynamics

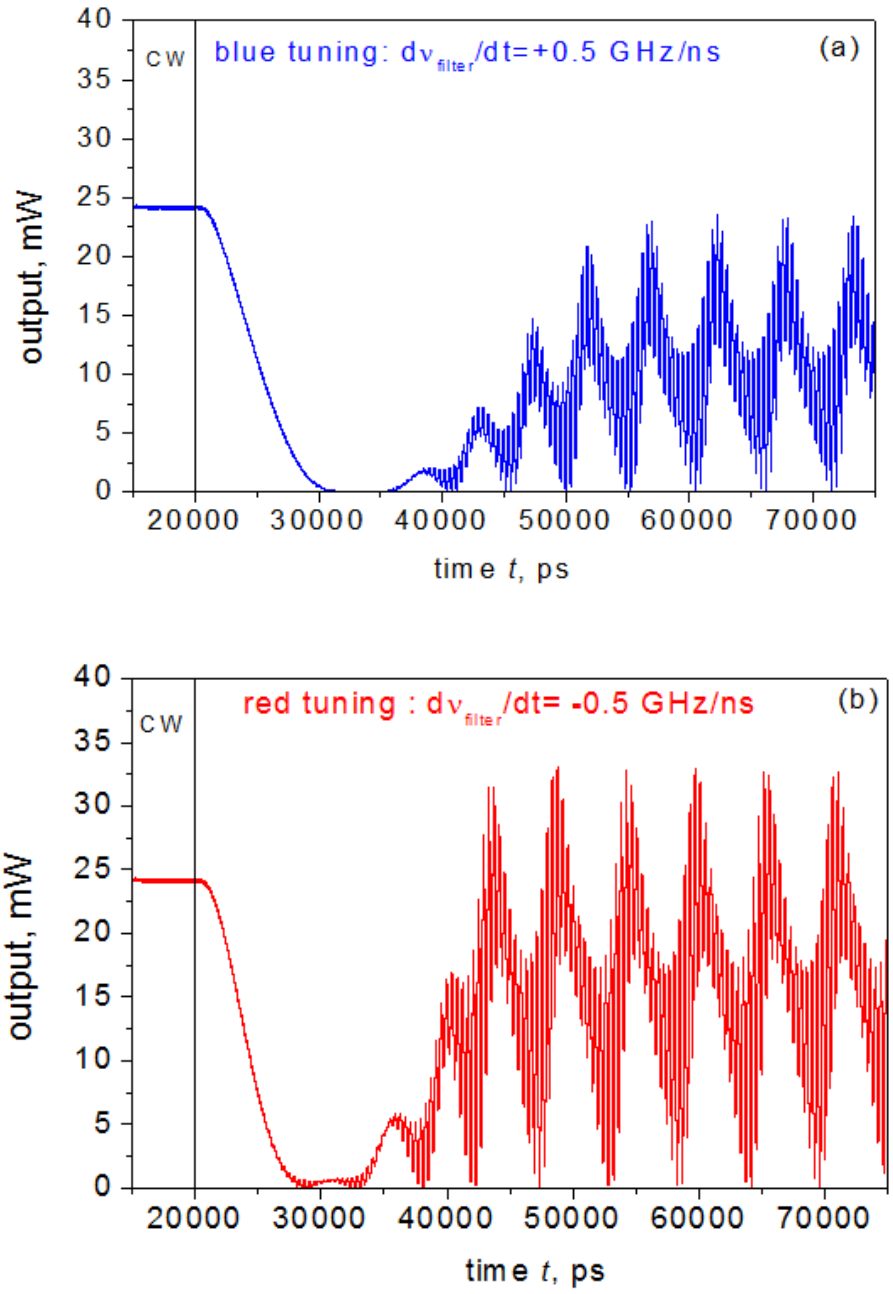

Figure 14 Transient power output of a swept source under blue (a) and red (b) tuning.

It is the left part of the graphs in which $t<t_{start} = 20ns$ a continuous wave (CW) simulated singlemode output can be found which is in agreement with experimental observations (Figures 14, left hand side of the curves)

We can see from both the blue (0.5GHz/ns) and red (-0.5GHz/ns) tuning a periodic or quasi periodic behaviour have formed after initial transient. This period of these variations ΔT is determined by intermodal interval/tuning speed, using the simple relation

$$\Delta T = \Delta \nu_{mod} \left(\frac{d\nu_{filter}}{dt} \right)^{-1}$$

$\Delta \nu_{mod}$ is the intermodal interval in GHz and $d\nu_{filter}/dt$ is the filter tuning speed in GHz/ns.

Qualitatively, similar behaviour is observed for both red and blue tuning. However, the average output power is noticeably lower at blue tuning than at red tuning, corresponding to a blue-red tuning asymmetry, similar to that obtained in the experiments and also in the simulations with ring lasers as discussed above. The origin of this asymmetry becomes clearer if we compare the power graph (Figure 18) with that of the corresponding instantaneous frequency which will be shown later.

This periodic dynamics has been found up to $d\nu_{filter}/dt$=-0.7 GHz/ns. But the periodic behaviour is gradually disappearing at higher tuning speed.

At the tuning speed of -0.8 GHz/ns the output power gives almost nothing at all on the dynamics graph. The laser suddenly switches off, as shown in Figure 15.

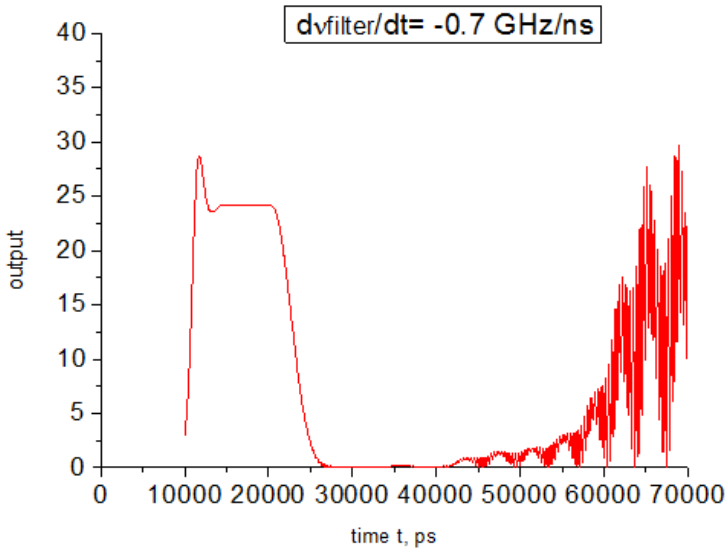

(a)

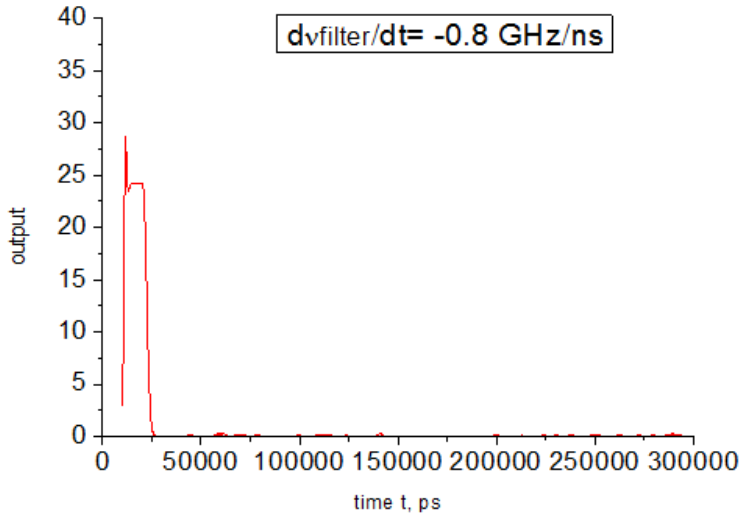

(b)

Figure 15 The absence of lasing output at high filter frequency tuning speed (red tuning). Note that a small change in the sweeping speed produces a large change in behaviour.

This sudden switching off also happened to positive tuning (Figure 16) to with a similar value of tuning speed at 0.7 GHz/ns given that filter bandwidth is 2GHz and alpha factor is 2. As we can see at the speed of 0.67 GHz/ns, the laser is still producing a periodic waveform although a similar output power vanishing from start as the red tuning.

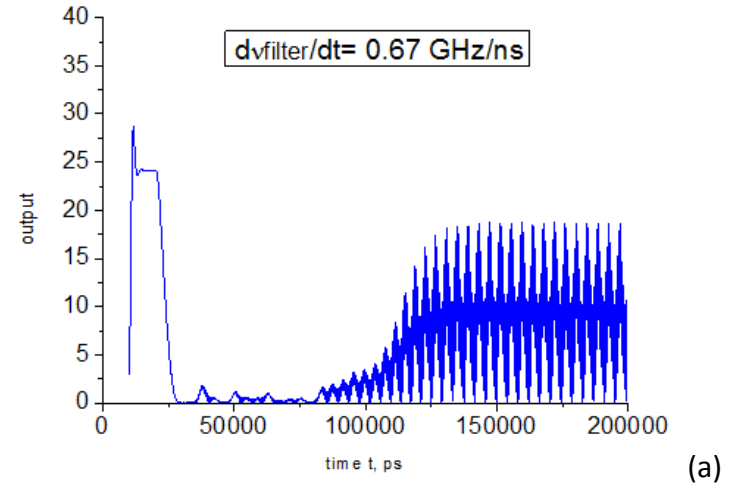

(a)

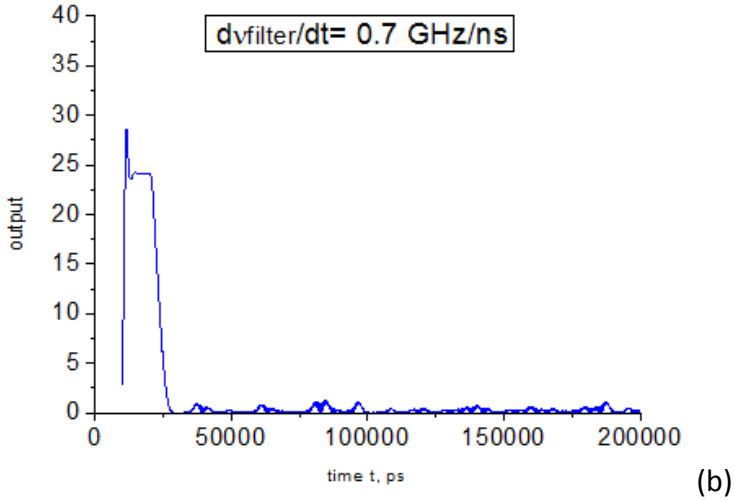

(b)

Figure 16 The absence of lasing output at high filter frequency tuning speed (red tuning)

5.2.2 Instantaneous frequency vs. time

To make clearer the nature of laser dynamics, we have plotted the dynamics of instantaneous light frequency during red and blue tuning.

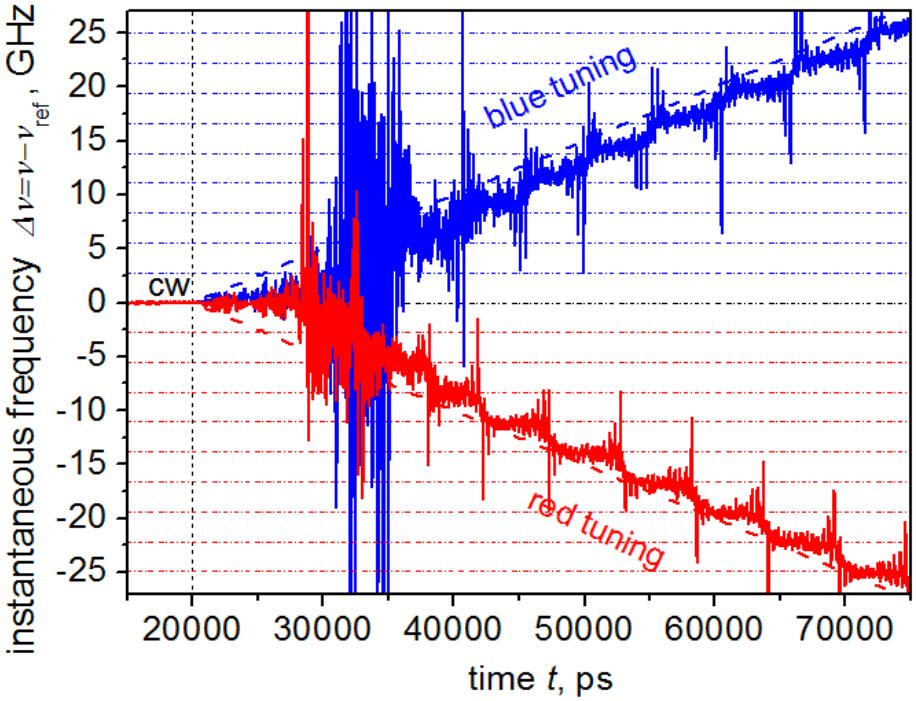

Figure 17 Time-resolved operating frequency of a swept source during the process of Figure 14 (filtered for clarity). Dashed lines: filter reflectance peak; horizontal dash-dotted lines: cavity modes.

The instantaneous frequency of the laser output can be expressed as

$$\Delta\nu = \frac{d}{dt} arg(E_{out})$$

where E_{out} is the slow amplitude of output light generated by the model.

The instantaneous frequency graph shows (after the time of about 40 ns) the same frequency intervals that can be seen in the quasi-periodic behaviour of the output power. Namely, we can clearly see that, although the output during each intensity variation period in laser dynamics Figure 14 is never *exactly* single-mode at this relatively high tuning rate, there is still one *dominant* mode during each period (the instantaneous frequency during most of each period is approximately following a horizontal line, which is close to the dash-dotted line which was drawn to represent the dominant

mode for every interval). The laser tuning is achieved in the form of mode hopping from one mode to another.

The two dashed lines are filter reflectance peaks for blue and red tuning, which the hopping instantaneous frequency is broadly following.

Since the filter bandwidth is 2 GHz, if the filter is not swept, the laser output in our output has a relative frequency of within about 2 GHz of the reference frequency. But since the start of the sweep of the filter, even though at each moment in time the wavelength is within 2 GHz (the filter bandwidth) of the current filter peak, on the whole a very broad range can be tuned. This is true for both blue and red tuning; however, we see that the position of the dominant mode stays closer to the filter reflectance peak, in the case of red tuning than in the case of blue tuning.

If is worth noting that, when the tuning speed is decreased, then the inter-hop period ΔT will be longer and the laser behaviour between frequency hops becomes nearer to true single-frequency operation. This means that both the power and the instantaneous frequency during the middle of each of the inter-hop periods are nearly constant, and the frequency is that of the mode.

Next, we proceed to calculate the dependence of the average power on the tuning speed, that is, producing a curve similar to that of Figure 6, but for the case of a Fabry-Pérot laser.

The output power was calculated by time averaging the output power at every tuning speed over a significant length of time. It must be noted that

choosing the time interval for such averaging is not trivial. In our calculations, we ignored the unstable periods at the beginning, the average power was calculated by averaging over an integer number of periods in the laser dynamics while they become stable. At very small tuning speed, only one or two periods have been generated. This could lead to a slight inaccuracy when taking the mean power. At higher tuning speed some regular periods will appear, taking average power from those periods does not have any obstacles and will be somewhat more precise than in the case of the lowest tuning speed values.

Figure 18 shows this dependence from our simulations. As in the case of ring lasers, and as can be expected from Figure 14, the asymmetry between the power for red and blue tuning can be clearly seen, with the average power being always higher for red tuning. Also as in ring lasers, the intensity falls with the tuning speed. In fact, above a certain critical tuning speed value, the laser does not switch on at all within the simulation span of 1 μs. The power drops quickly at small tuning speed then falls gently while the speed increases. When the filter is swept too fast passing the modes, there is no time for the modes to build up, the output power suddenly drops to 0.

This is what happens at each end of the diagram. So in that case, the laser does not switch on at all. It happens at the tuning speed range of 0 to 0.8 GHz/ns. This is in agreement with an estimate of up to ~ 1 GHz/ns from the simple consideration of each mode needing a few roundtrips to build up in the spectrum.

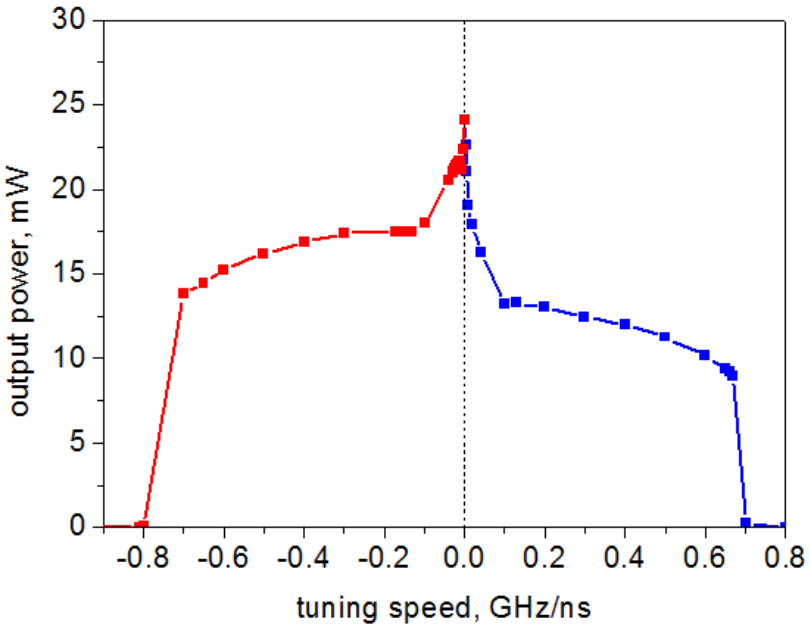

Figure 18 Tuning speed dependence of the output power.

The asymmetry as present in the above figure is associated with the asymmetric mode interaction due to the nonzero linewidth enhancement factor in the laser. This behaviour was found in the case of ring laser as well. [20] The origin of asymmetry is the asymmetric mode interaction due to Henry factor, sometimes called the Bogatov effect. It was first studied by Bogatov and co-authors in 1975. [26]. It is a result of carrier pulsations due to mode beating, which lead to periodic oscillations of the optical properties of the material. The asymmetric nature of this modal interaction is due to linewidth enhancement factor or Henry factor α_H. In the process of modal interaction, a weak mode next to the powerful mode is helped if it is on the red side, and suppressed if it is on the blue side. So with red tuning each old mode helps the new mode to be build up, whereas with blue tuning, the old mode tries to suppress the new mode.

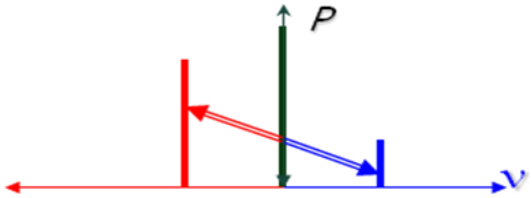

Figure 19 Schematic representation of asymmetric mode interaction due to linewidth enhancement (Henry) factor α_H; for two modes, strong and weak

According to their results [26], the correction to the gain of the weak mode due to the presence of the strong mode can be expressed as:

$$\Delta g_{weak} = -g_0 \varepsilon_X \frac{1-\alpha_H \left(\omega_{strong} - \omega_{weak}\right)\tau_{recombination}}{1+\left(\omega_{strong} - \omega_{weak}\right)^2 \tau_{recombination}^2} P_{strong}$$

where ε_X is the gain cross-compression coefficient due to population pulsations, $\tau_{recombination}$ is the total (stimulated and non-stimulated) recombination time of carriers, and the ω_{strong} and ω_{weak} are the optical frequencies of the strong and weak modes, P is the optical power, and g_0 is the small-signal gain.

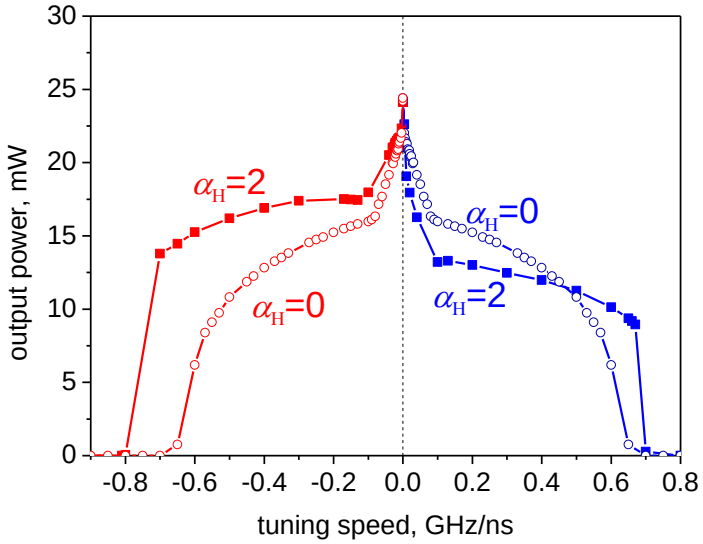

Figure 20 Tuning speed dependence of the output power in the presence and in the absence of self-phase modulation.

The previous curves of output power against tuning speed (Figure 18) have been calculated with α_H=2; Figure 20 shows the same curve alongside the similar result of zero Henry factor, α_H=0. Similar procedures were made when calculating the mean output power for every tuning speed that is available in dynamics. We found that the data in output files for red and blue tuning are exactly the same. As a result, the curves of the two tuning speed becomes completely symmetric.

From the figure we can see that the average power for red tuning is above the α_H=0 curve and below the zero Henry factor curve for blue tuning. It is also an indication of the Bogatov effect.

We believe the results presented above show a fairly comprehensive picture of the behaviour of the laser with a narrow filter bandwidth. However, as the

analysis is numerical rather than analytical, it is not obvious to what extent the behaviour of a construction with a broader filter bandwidth will be similar.

5.3 Dynamics of the laser with a broadband filter

We analyse next the case of filter bandwidth of 20 GHz, and the alpha-factor of 2 holds,

$$\delta\nu_f = 20 \text{ GHz} > \delta\nu_{\text{intermodal}} = 2.7 \text{ GHz}$$

so that the filter bandwidth is broader than the intermodal interval which is 2.7GHz and 10 times broader than the previous narrow filter bandwidth. This might give a good comparison in the later investigations.

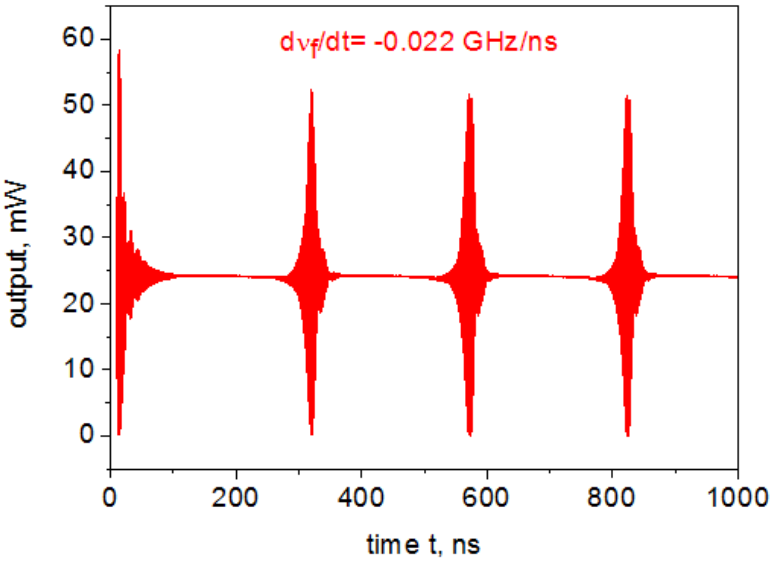

Figure 21 Power output profile for a broadband filter; the tuning speed is -0.022 GHz/ns

When filter bandwidth is greater than intermodal interval. At very small tuning speed, -0.022GHz/ns we see only 3 to 4 periods are emerged within

the tuning span of 1μs, which means only 3 or 4 modes are tuned by the filter. This small number of variation periods can be explained by the previously-stated relation showing the period of quasi-periodic oscillation to be equal to, or near, the intermodal interval/ tuning speed ratio (and independent on the filter bandwidth), where the intermodal interval $\Delta\nu_{mod}$ is fixed at 2.7 GHz.

It can be observed that the mode hopping dynamics is similar to narrowband filter and the number of modes is increasing as filter tuning speed increases. At tuning speed of -0.05GHz/ns, more modes can be seen.

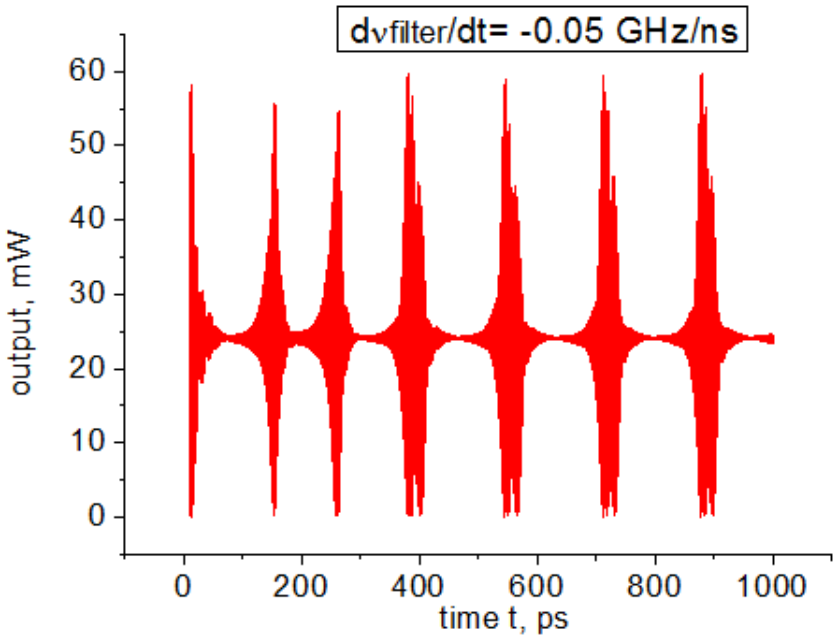

Figure 22 Power output profile for a broadband filter; the tuning speed is -0.05GHz/ns

As the tuning speed increases, the number of modes increases too, some irregular multimode dynamics appears in the output of the laser. (Figure 23)

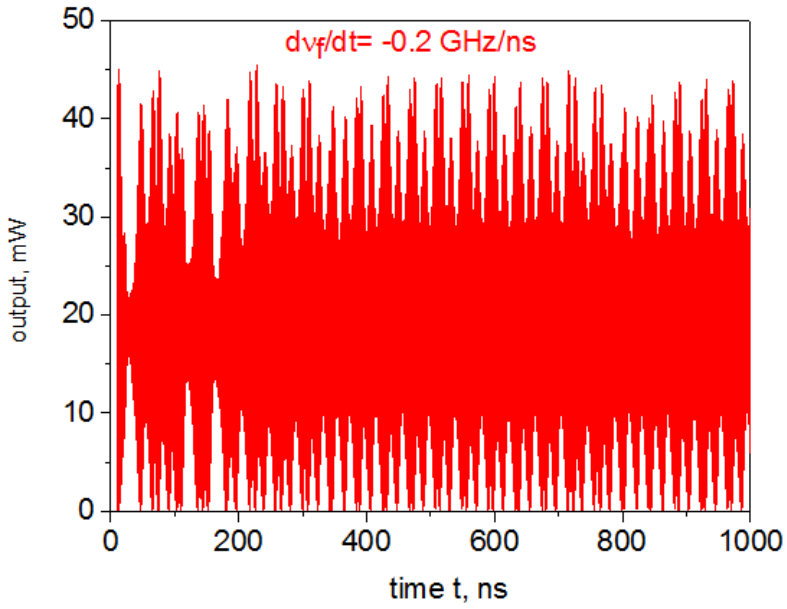

Figure 23 Power output profile for a broadband filter; the tuning speed is -0.2GHz/ns

As filter tuning speed continue to increase to -0.6GHz/ns, under some conditions the powers experience considerable transient variations, decreasing almost to zero before 150 ns and then increasing dramatically from 50 mW to over 100 mW, but back to 50 mW after 150ns. From time 200 ns in this case, peak powers of laser dynamics stay in a line at around 50 mW (Figure 24 a)

It is this steady part of the graph that is indicative of the laser behaviour during tuning; we therefore take a close look at it, as shown below in (Figure 24 b). A regular structure of laser dynamics appears here; a similar periodic structure was noticed at a broad interval of high tuning speed of red tuning. The repetition period was found to be half of the round-trip time of laser cavity; in other words, there are *two pulses* for each repetition period.

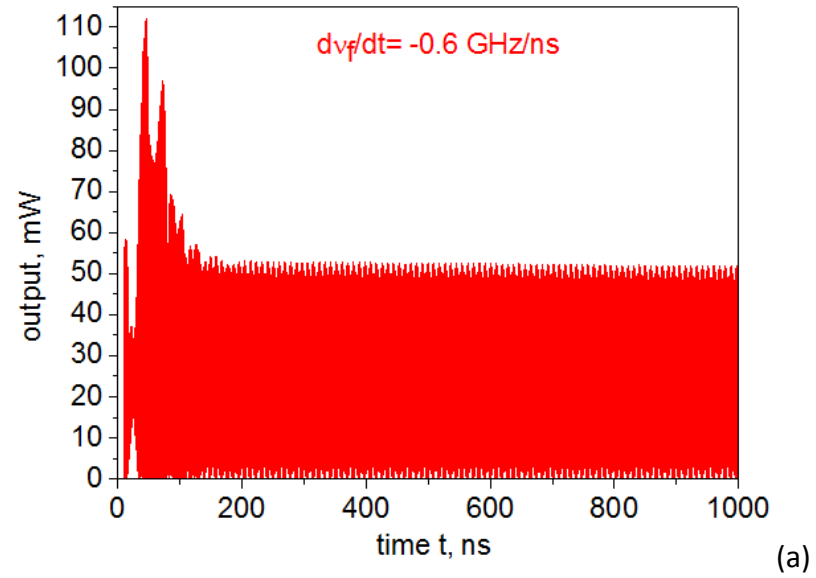

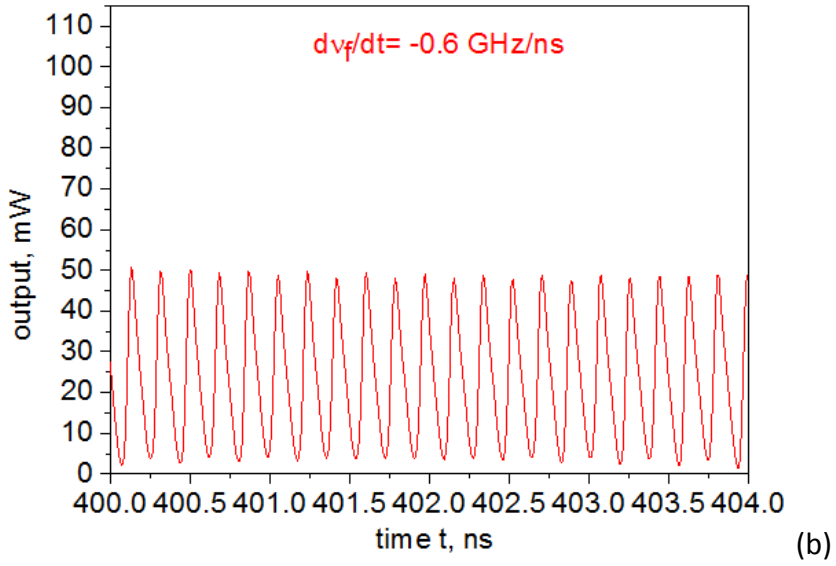

Figure 24 Power output profile for a broadband filter; the tuning speed is –0.6 GHz/ns

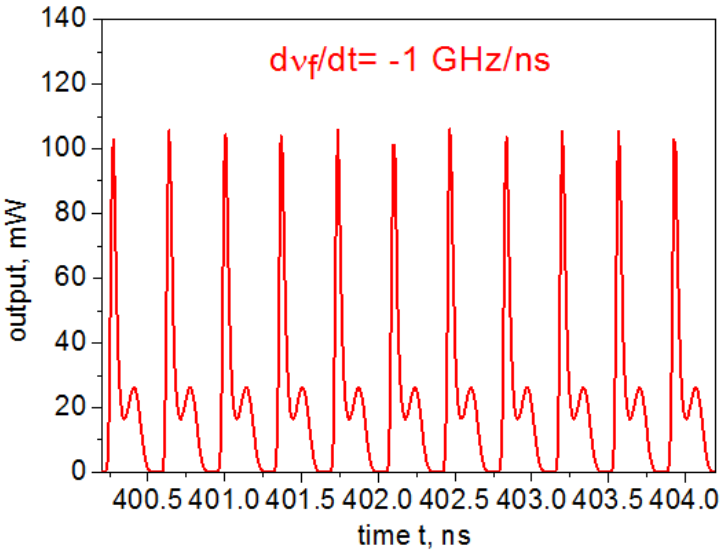

Figure 25 Power output profile for a broadband filter; the tuning speed is –1 GHz/ns

So there are 2 pulses with almost the same peak power within one round trip in the previous figure 24.

If we increase the tuning speed further to -1GHz/ns (Figure 25), we see "period doubling" in the laser dynamics compared to that of -0.6GHz/ns (Figure 24). There are still two pulses in one round trip time, but one of the two pulses becomes weakened, so there is one pulse smaller than the other which sits next to it.

With a further increase in tuning speed, those smaller pulses are gradually disappearing, leaving only one pulse per period.

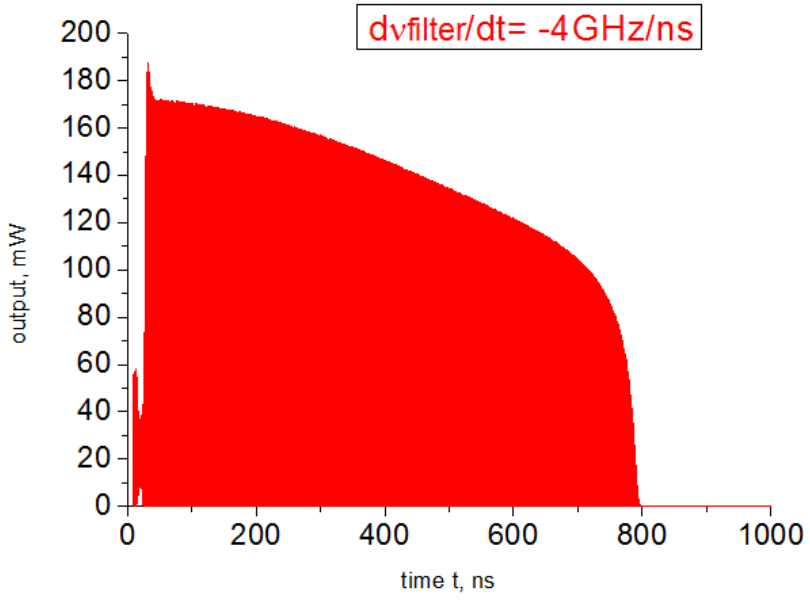

(a)

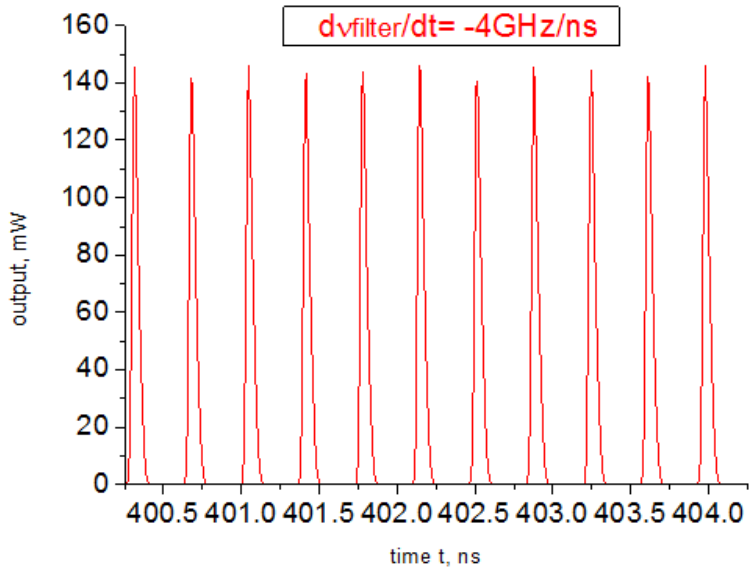

(b)

Figure 26 Power output profile for a broadband filter; the tuning speed is –4GHz/ns

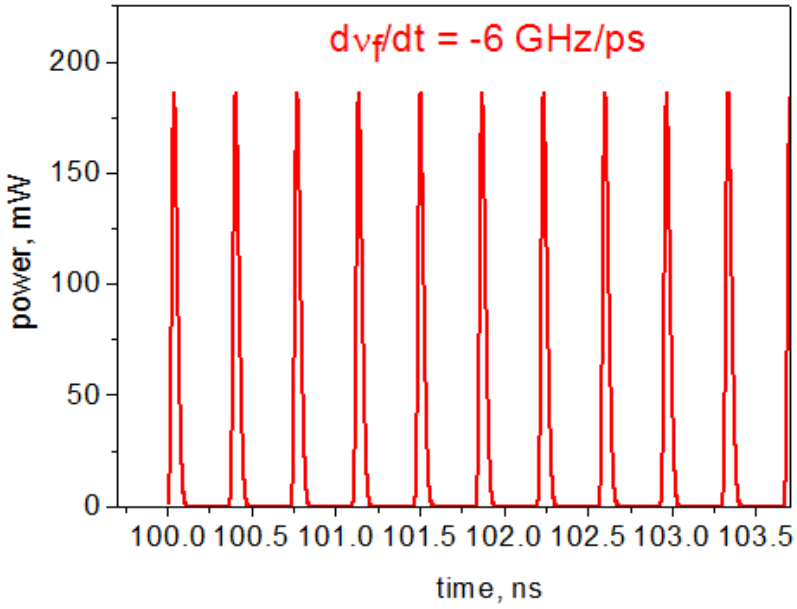

Figure 27 Power output profile for a broadband filter; the tuning speed is –4GHz/ns

At very high tuning speed of -4GHz/ns, up to -6GHz/ns, the period doubling compared to the situation considered above is complete; the weaker pulses in each period have completely disappeared, leaving only the stronger pulses, therefore a regular short pulse train is generated in this occasion.

The repetition period at high tuning speed -4GHz/ns as shown is the round trip time of laser cavity. (Figure 26 (b))

Thus at very high tuning speed, a sequence of short pulses (with a full width half maximum (FWHM) of 38 ps in the case simulated above) has been found at the round trip repetition rate.

On a long time scale, there is noticeable decay in pulse amplitude in Figure 26 (a), eventually rolling down to zero. This is due to the fact that the laser is detuned away from the gain peak, effectively reducing the current over threshold (see more detailed discussion below); when the current dips

below threshold for the instantaneous detuning value, the laser switches off. If there was no gain dispersion in the model, the laser output *intensity* (power) behaviour would be ideally periodic.

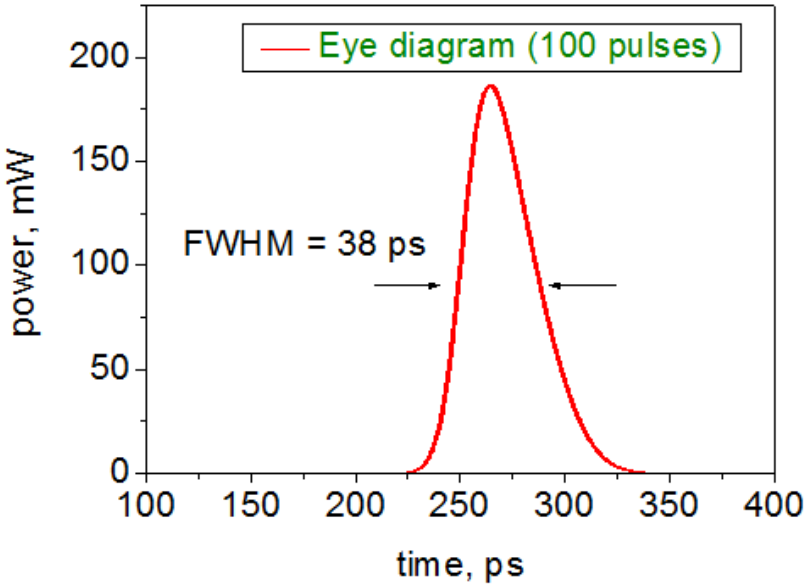

Figure 28 Eye diagram of 100 short pulses for tuning speed of -6 GHz/ns

This type of laser operation (periodic emission of short pulses, with the period equal or near the cavity round-trip) is usually called *mode locking* behaviour. Since our laser has no saturable absorber and no resonant modulation is applied, it would have to be classified as *self mode locking*.

In order to check that the intensity variation of this regime is really periodic (a feature of mode locking), we have plotted (Figure 28) an eye diagram of 100 short pulses for tuning speed of -6 GHz/ns. The pulses are taken from the start of the tuning curve (running time < 100 ns), so the effect of detuning from the gain maximum is not yet visible. The eye diagram is found to be quite open, which shows the intensity behaviour is quite periodic and can indeed be described as (self)-mode-locking.

But this mode-locking is somewhat unusual. Not only is it self-mode locking instead of the more usually observed active or passive mode locking. There is another important difference. In ordinary mode locking, not only is the intensity variation periodic with the round-trip period, the phase behaviour of the laser is periodic as well. In our case, however, the pulsating behaviour is caused by tuning, so the phase behaviour of each pulse (the instantaneous frequency during the pulse) is different from the previous pulse.

To illustrate this, we have plotted as dots the relative instantaneous frequency calculated at every pulse peak from 0 to 150 ns. It is clearly seen that, as can be expected, the central frequency of those pulses change gradually from pulse to pulse. As time is passing, the central frequency of pulses decreases from 0 to near -800 GHz, since waves only within the band of 20 GHz around the filter maximum are reflected back. These frequencies follow the filter reflectance peak and we observed so as well, see figure (29) below. The blue dashed line is the filter reflectance peak. It can be seen that the 100 pulses cover about 36 ns and their centre frequencies are tuned over time.

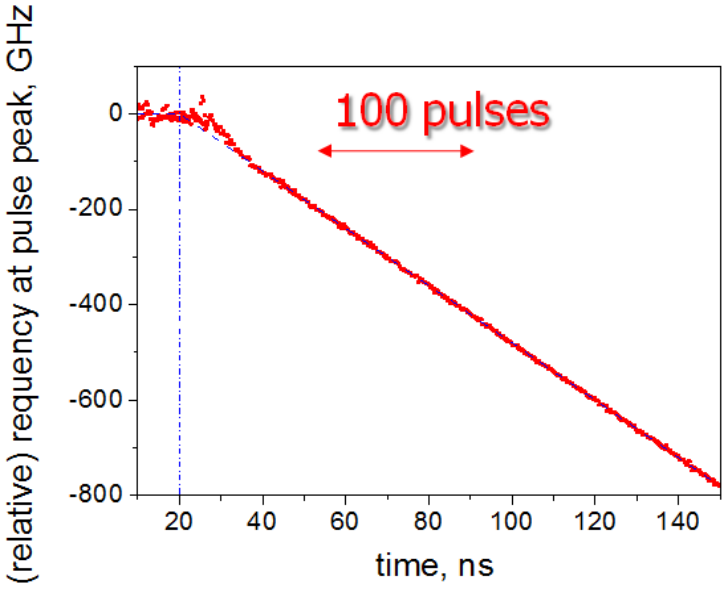

Figure 29 Instantaneous frequencies at the peak of "self mode locking" pulses (red dots) as function of the tuning time. The blue dashed curve is the position of the filter peak.

5.4 Properties of the "mode locked" type pulses

Figure 30 shows that in the right-hand-side the spectrum of a single pulse, say pulse number *N*, is the single pulse taken from one of the mode locking dynamics at 6GHz/ns.

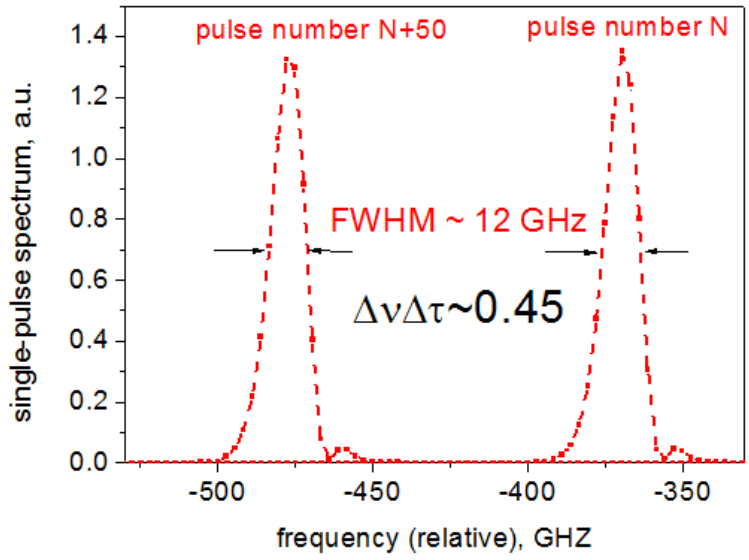

Figure 30 single pulse spectrum of number N and N+50

The spectral width of this pulse (measured as Full Width at Half Maximum, FWHM) is 12GHz. In this regime, we use this spectral width as an estimate for the instantaneous linewidth that relates to the coherence length in OCT which determines the scan imaging depth in the tissue:

$$\textbf{Coherence Length} = \frac{\mathbf{C}}{\mathbf{linewidth}}$$

As we move to the next pulse which is 50 pulses away from pulse Number N (left-hand-side of the figure), it can be seen that the single-pulse spectral width keeps constant (as does the lineshape), so the single-pulse spectrum from pulse to pulse is the same. However, the single pulse spectrum shifts in central frequency, as can be seen from the Figure (30), it shifts about 100 GHZ to the left, following the filter tuning.

The spectrum is not exactly symmetric because of the chirp (the instantaneous optical frequency shift during the optical pulse); the chirp is known to lead to a significant broadening of signal linewidth. In this case, the time-bandwidth product is 0.45. However, it is not too far from transform-limited with α_H=2. As we found from simulations setting α_H=0 (discussed in more detail below), the time-bandwidth product for unchirped pulses of this shape is 0.39, so 0.45 is not much greater, therefore, the chirp is not strong for the relatively modest Henry factor of α_H=2 that we use in our simulations.

5.5 Blue tuning for 20GHz filter bandwidth α_H=2

We then investigated the case of blue tuning of a broadband filter operated laser, to see if there are significant differences from red tuning.

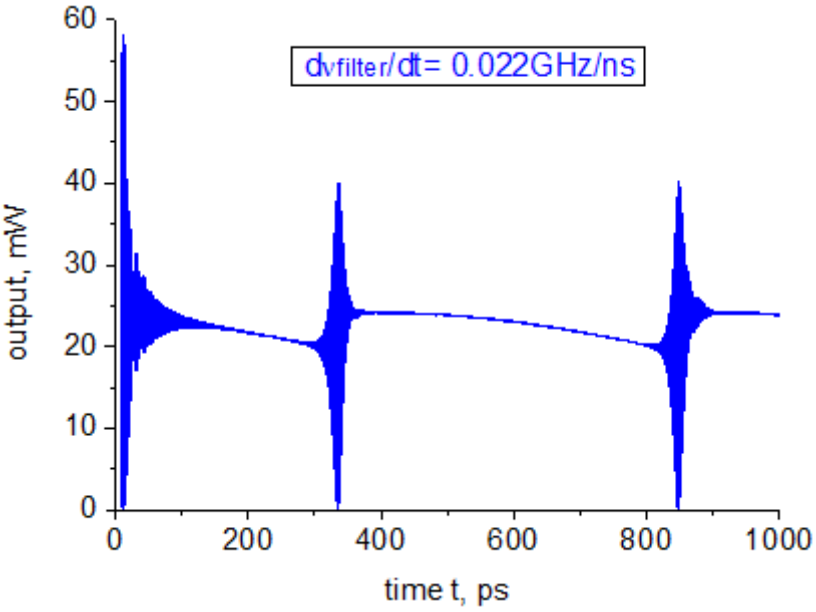

Figure 31 Power output profile for a broadband filter; the tuning speed is 0.022GHz/ns

At a very slow tuning speed of 0.022GHz/ns, only two notable modes are forming; this is similar to the red tuning case.

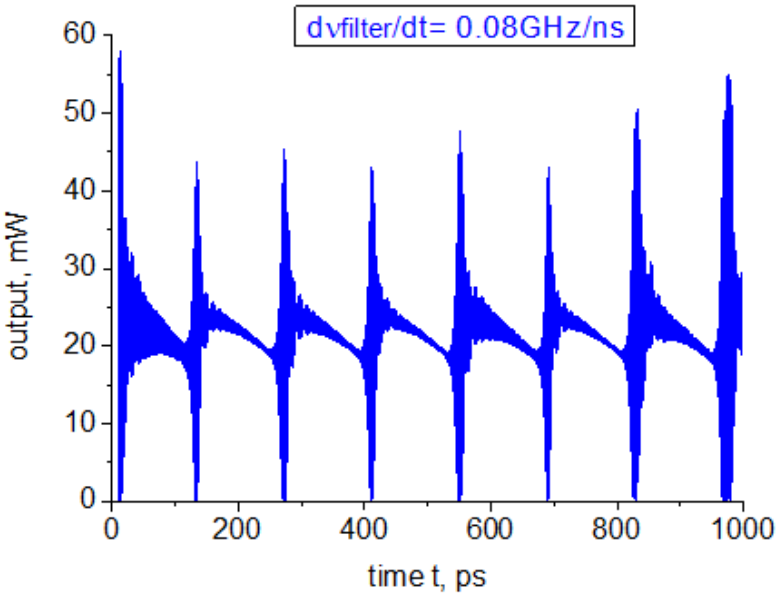

Figure 32 Power output profile for a broadband filter; the tuning speed is 0.08GHz/ns

With the increasing tuning speed, it can be seen from the above, figure 32 a variation period is forming, also not too different from the red tuning; the only relatively modest difference is that the power within the period is decreasing while pulses for red tuning at small tuning speeds it tends to stay roughly constant for each nearly-single-mode period.

At higher tuning speed of 1 GHz/ns, we find that the laser behaviour acquires a pulsating nature. In the case presented below, there are 3 broad “pulses” (corresponding to 2-3 modes in the instantaneous spectrum) in one round trip time of 361 ps. However, unlike the case of red tuning, these “pulses” are not stable, there is clearly some envelope dynamics.

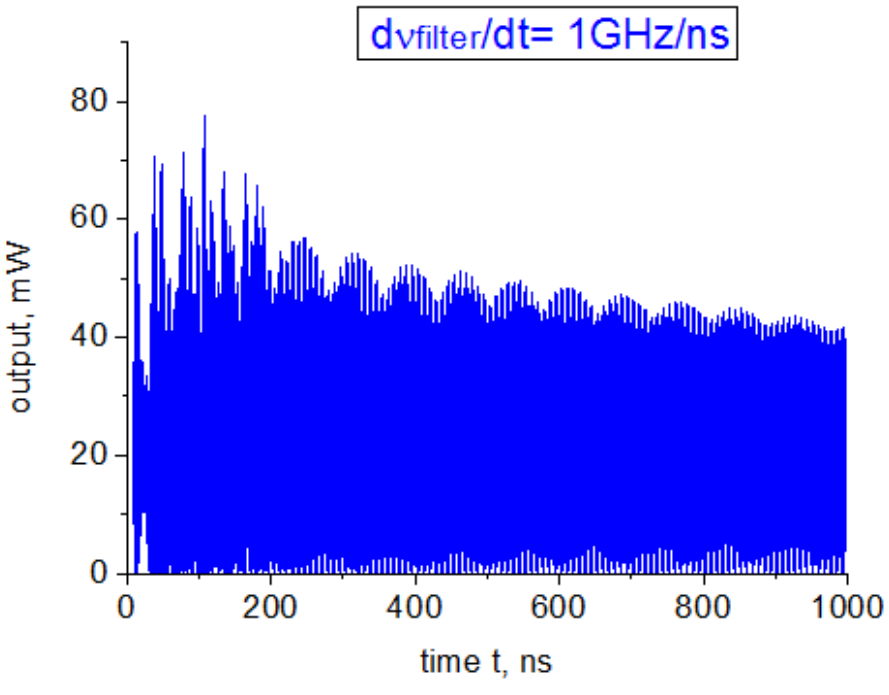

(a)

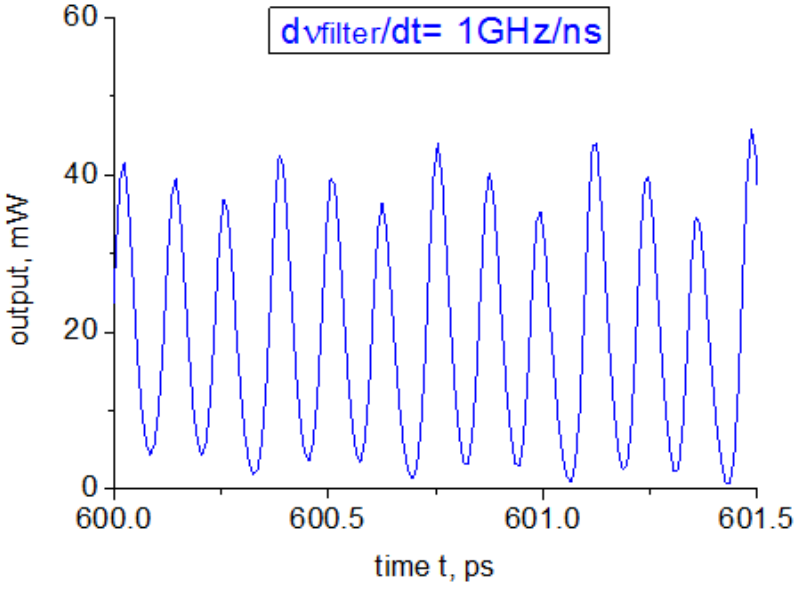

(b)

Figure 33 Power output profile for a broadband filter; the tuning speed is 1GHz/ns

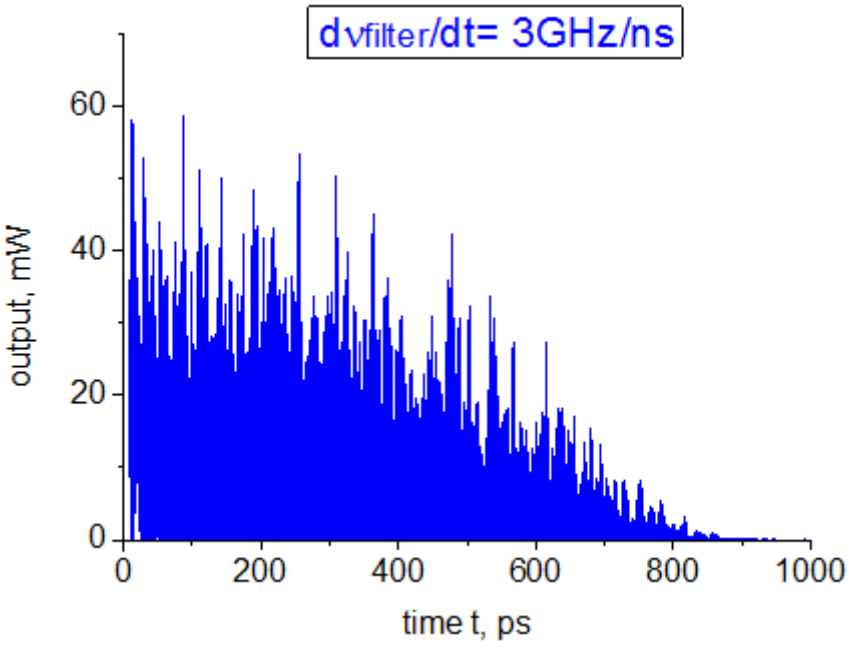

Figure 34 Power output profile for a broadband filter; the tuning speed is 3GHz/ns; current I/I_{th}=2.2

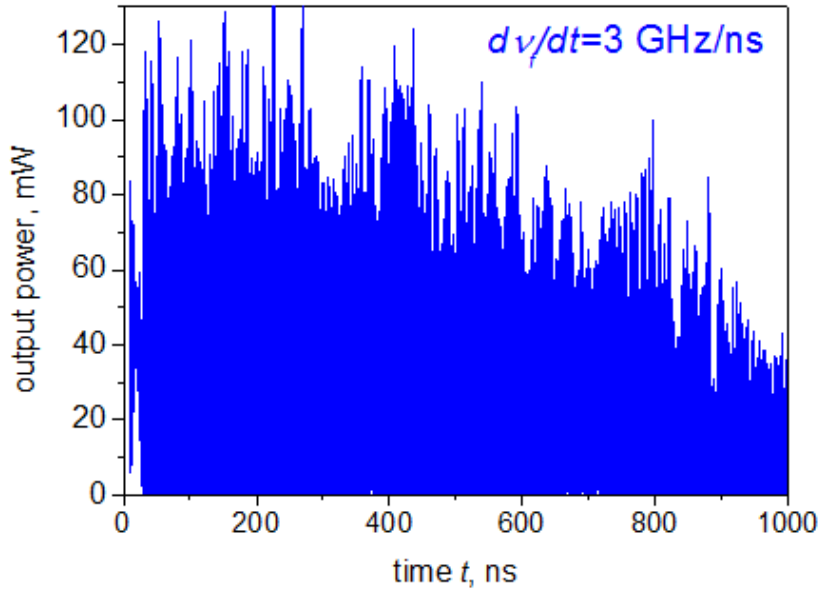

Figure 35 Power output profile for a broadband filter; the tuning speed is 3GHz/ns, current I/I_{th}=3.2

The main difference is seen as the blue tuning speed increases further still, to values of several GHz/ns. In this case, we see no regular sequence of short pulses; the light output is in the form of irregular bursts rather than regular pulse stream. Thus, for blue tuning with nonzero Henry factor, the dynamics is irregular, there is no self mode locking behaviour of the type observed for the same high speed at red tuning.

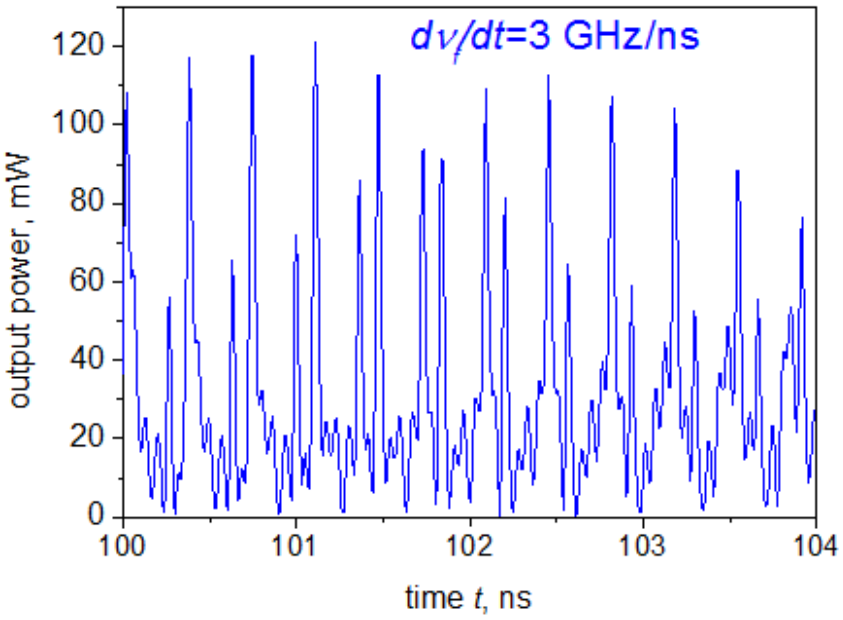

Figure 36 detailed Power output profile for a broadband filter; the tuning speed is 3GHz/ns, current I/I_{th}=2.2

5.6 Dynamics with broadband filter: effect of linewidth enhancement

We then analyse the behaviour of the construction with a filter bandwidth of 20GHz and α_H=0.

We find that in this case, there is an area of self-mode locking type behaviour and the power transients of negative and positive tuning are exactly the same with tuning speed of different signs; in other words, the power output against tuning speed is completely symmetric.

The pulses look periodic at -1/1 GHz/ns, regular pulses appear the repetition period is half of the round trip time of laser cavity.

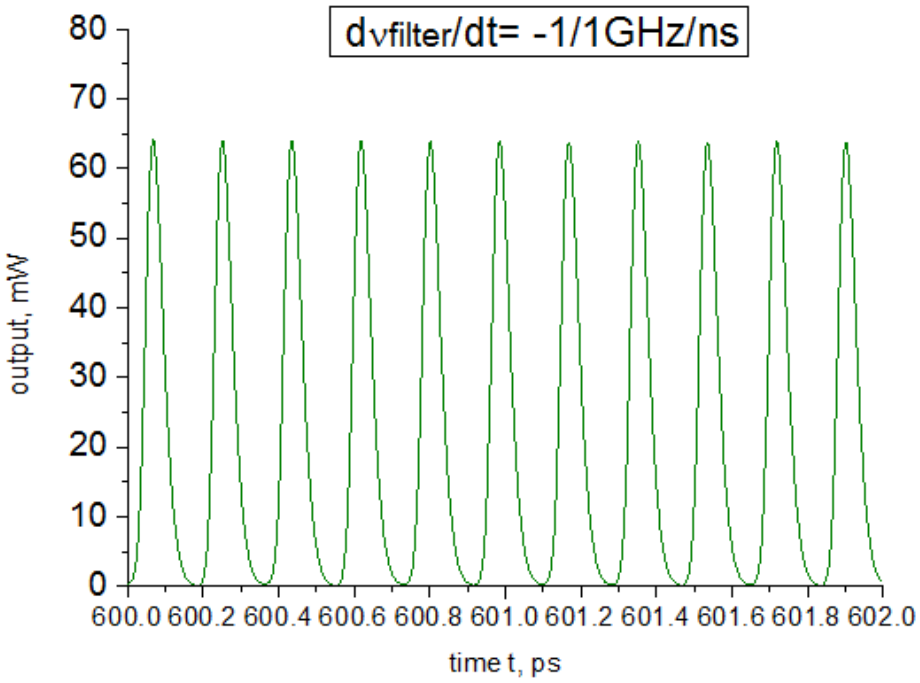

Figure 37 Power output profile for a broadband filter; the tuning speed is -1/1 GHz/ns

The laser switches off at large detunings (in this case, about 2.4 THz) due to the effects of gain curve.

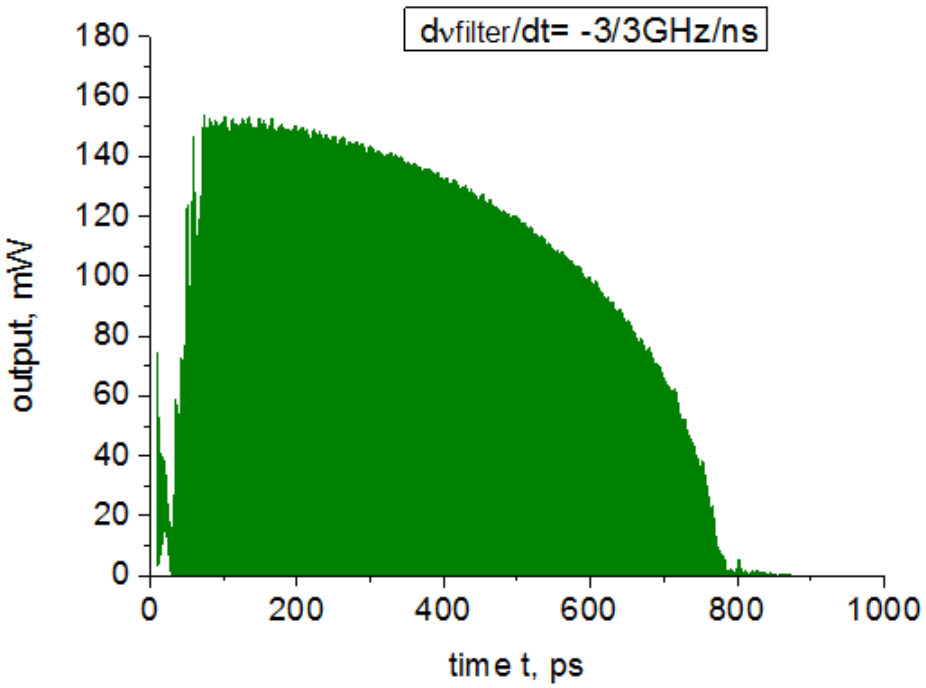

Figure 38 Power output profile for a broadband filter; the tuning speed is -1/1 GHz/ns

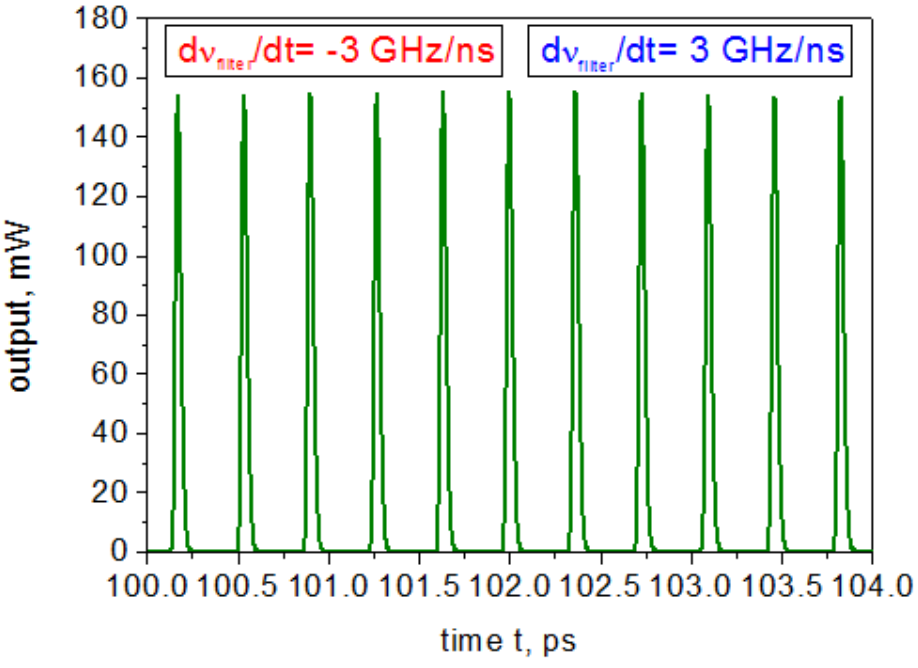

Figure 39 Power output profile for a broadband filter; the tuning speed is -1/1 GHz/ns

The laser dynamics for this high tuning speed are periodic with the period equal to round trip time. The mode-locking type regime are present also at α_{Henry}=0 as for α_{Henry}=2 for 20 GHz filter bandwidth. At all tuning speeds, we found that the blue and red tuning are exactly symmetric as expected.

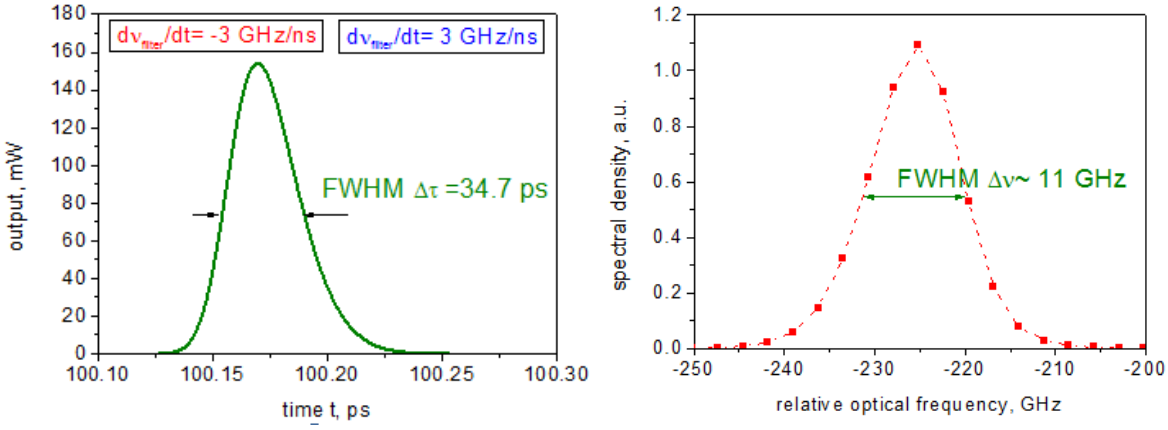

(a) (b)

Figure 40 Single-pulse shape (a) and spectrum (b) for a broadband-filter laser, in the absence of self phase modulation (α_H=0).

The spectrum of a single pulse at tuning speed of -3 GHz/ns or 3 GHz/ns (they have the same spectrum) is quite symmetric for the case of no alpha factor, which is indicative of little or no chirp. However, it can be seen from the pulse profile, Figure 40) that pulse shape itself is still noticeably asymmetric. The time-bandwidth product is $\Delta\nu\Delta\tau$=0.39, which we take to be the transform limit for this pulse shape, compared to 0.31 for *Gaussian* unchirped pulses.

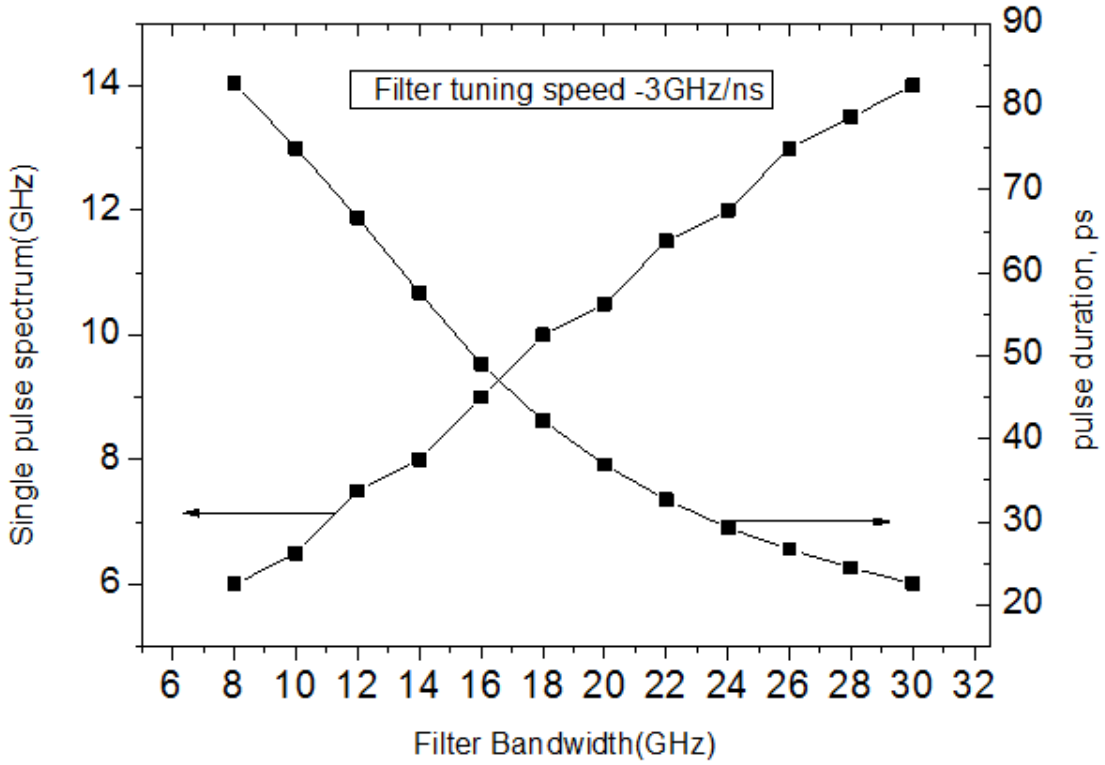

Figure 41 Filter bandwidth dependence on the pulse amplitude and instantaneous linewidth. Red tuning speed -3 GHz/ns; linewidth enhancement factor α_H =2,

To study the characteristics of output power pulses further, a broad range of filter bandwidths has been investigated for a fixed tuning speed.

Figure 41 shows the single pulse spectrum is in a trend of declining when filter bandwidth increases. The pulse duration is getting wider with the increasing filter bandwidth. A bandwidth narrower than 6GHz will give no pronounced pulsing behaviour in the output power transient for the case of -3GHz/ns filter tuning speed.

We proceed with plotting the curves of average output power vs. tuning speed, in the same manner as did earlier for the narrowband filter. The results are plotted in Figure 42 (solid lines), with the results for a laser

with a narrowband filter plotted alongside, for comparison, as dashed lines.

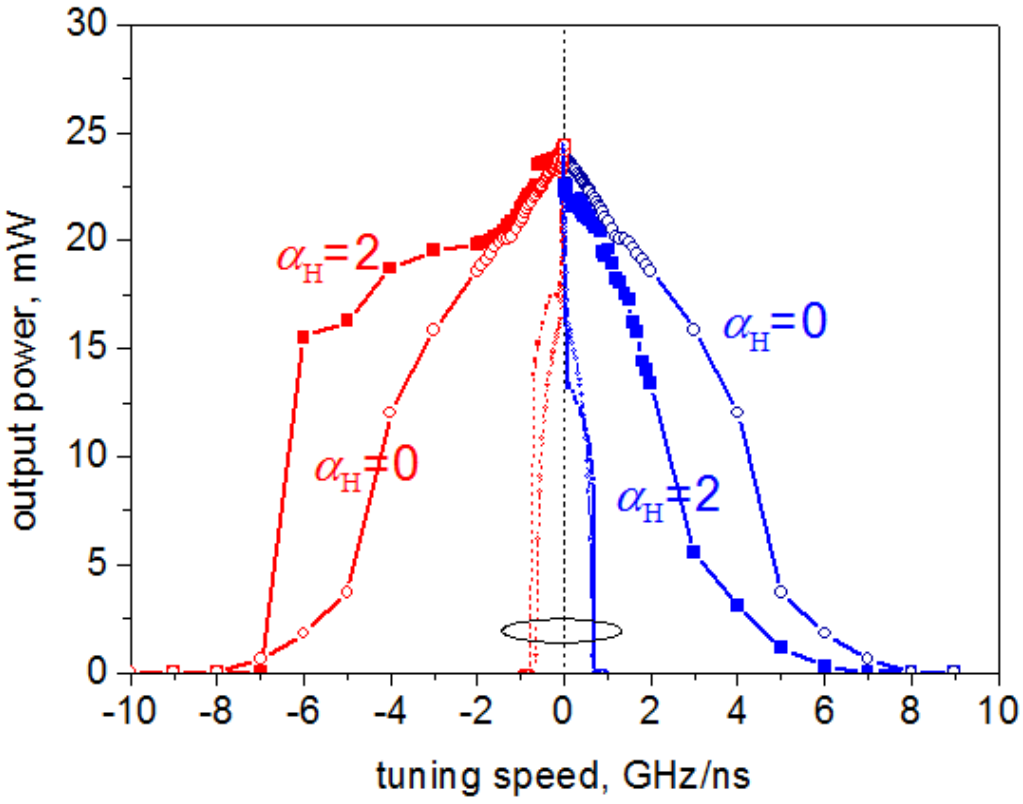

Figure 42 The tuning speed dependence of the average optical power. Solid curves with symbols: broadband filter. Doted curves: narrowband filter (for comparison). Filled symbols: with self phase modulation (Henry factor αH =2). Empty symbols: no self phase modulation (Henry factor αH =0).

Comparing the results for the narrowband and broadband filter, we find that the characteristic filter tuning speed $d\nu_f/dt$ at which the laser power drops scales *roughly* proportionally to the filter bandwidth $\delta\nu_f$, as expected. It is however not exactly ten times since mode interactions are different in the case of a broadband filter from the case of a narrowband filter, and mode interactions affect the possible tuning speed. The laser switches off at less than +/-1 GHz/ns with a 2 GHz filter bandwidth and the same situations happens at +/-8 GHz/ns for a 20 GHz filter bandwidth.

If α_H>0, laser tuning is asymmetric. It has also concluded that the range of tuning speed for red tuning is broader than that of blue tuning.

Finally, we address the issue of the total tuning range in terms of optical frequency, briefly mentioned before. We find that this range is *roughly* similar for blue and red tuning, and for all tuning speeds. However, there are modest but noticeable differences depending on the tuning speed and direction. As shown in the figure 42 below, the red tuning range for α_H=2 is of the order of about 3.2 THz, the blue tuning range slightly smaller, about 2.3 THz, which is also close to the red and blue tuning range of a laser with α_H=0, as discussed above.

Wavelength tuning range with broadband filter

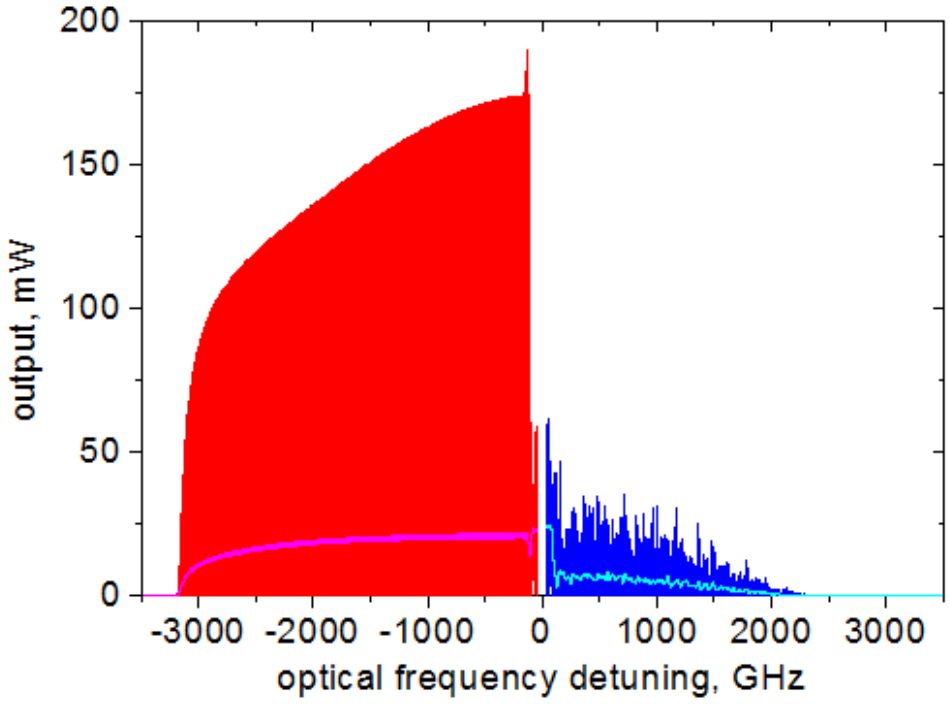

Figure 43 The tuning range of the laser with a broadband filter, calculated by a combination of red and blue sweeping. The light coloured curves show the time-averaged power

The probable explanation for this behaviour is as follows.

The tuning range in terms of optical frequency is determined coarsely by linear effects and finely by nonlinear effects

The linear effects are gain spectrum and operating current. When we detune the laser too much from gain peak the threshold current increases and then the pumping current becomes below threshold. The laser then switches off approximately when the condition

$$I \approx I_{th}(\Delta\nu),$$

is satisfied, as illustrated in the figure below. However, in practice this is slightly modified by the nonlinear effects.

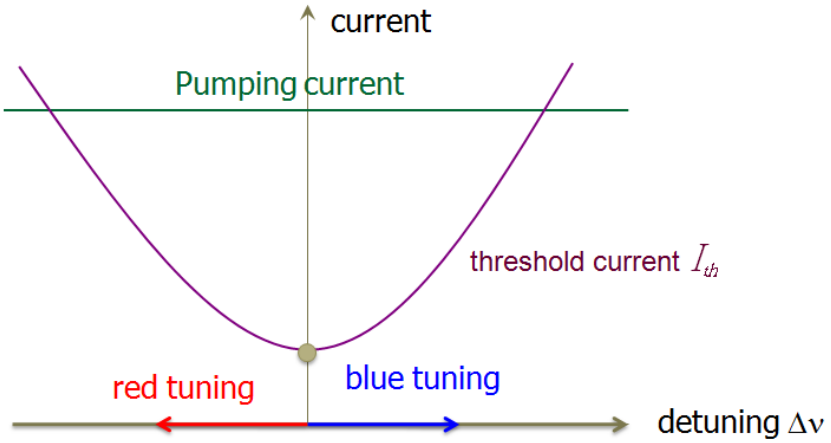

Figure 44 Schematic illustration of the main physical reason of laser power decay and eventual switch-off with detuning.

The nonlinear effects of interest here are the modal interactions, which lead to the mode locking type behaviour and are different for different Henry factor values and tuning direction and speed. Because the small correction that makes the tuning asymmetric comes from mode interaction, the red tuning range becomes longer than the blue tuning.

5.7 Dynamics of a long laser cavity

To get a more general view of the dynamics of a long laser cavity, we increase the cavity length by a factor of 5, while setting the filter bandwidth to 4GHz, in order to ensure the same number of modes within in the filter bandwidth as the initial simulations with a 20 GHz filter bandwidth.

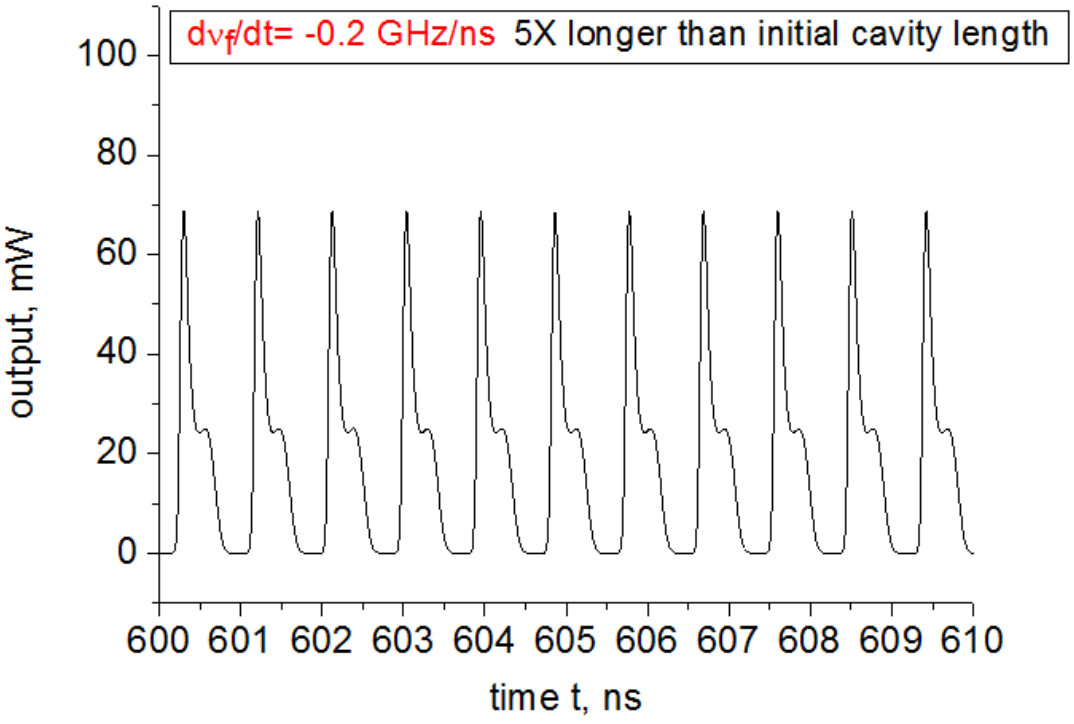

Figure 45 Power output profile for a broadband filter longer laser cavity; the tuning speed is -0.2 GHz/ns

With a laser cavity length of 5 times longer than the initial length 1.5498 cm in semiconductor material, we can still see the quasi-stationary, “self mode locking” behaviour; however, we did not observe true short pulse generation, only broader structures of the type shown in Figure 45.

Similar structures, though less regular and even less reminiscent of mode locking pulses, have been observed previously in a ring laser which has a much longer resonator [20].

6 Conclusions

The following conclusions can thus be made from our simulations:

- Simulations show that the experimentally observed asymmetry in the behaviour of the FP laser is the result of asymmetric mode interaction. This is similar to the conclusions made by previous authors [20] on ring lasers.

- For more symmetric tuning behaviour, it would be necessary to reduce the (effective) alpha factor of the laser. Some methods of doing so have been proposed by the authors of , [20] and involve the use Quantum Dot/Dash lasers near threshold, when the alpha-factor is low, On the other hand, the alpha-factor of QD lasers is known to increase with bias, so this is no very reliable method. It may be also attractive to use multisection lasers, for example with saturable absorbers, where the self phase modulation in the gain and absorber section can cancel each other. Such a laser may operate in a mode-locked regime for both blue and red tuning.

- The dynamics of short and long cavity (or narrowband and broadband filters, which is more or less the same) have been shown to be quite different, in general – though the broadband filter for very slow tuning is similar to the narrowband filter.

- The difference in the regularity of tuning in red and blue directions has been shown to be due to qualitatively different dynamic regimes. A new dynamic regime has been observed under fast red tuning with a broadband filter: self mode locked type behaviour with periodic intensity but swept central frequency.

7 List of abbreviations

continuous waveform (CW)

Fabry-Pérot (FP)

frequency- domain OCT (FD-OCT)

high-reflection (HR)

full width at half maximum (FWHM)

Micro-Electro-Mechanical System (MEMS)

Multi-Quantum Well (MQW)

Optical Coherent Tomography (OCT)

quantum dot (QD)

reflective Fabry-Pérot tunable laser (RFPTL)

semiconductor optical amplifier (SOA)

signal-to-noise ratio (SNR)

swept-source OCT (SS-OCT)

8 References

1. Huang, D., Swanson, E.A, Lin, C.P., et aI., Science, 254: 1178-1181 (1991).
2. A. G. Podoleanu, M. Seeger, G. M. Dobre, D. J. Webb, D. A. Jackson, and F. W. Fitzke, “Transversal and longitudinal images from retina of the living eye using low coherence reflectometry,” J. Biomed. Opt., vol. 3, pp. 12–20, 1998.
3. B. M. Hoeling, A. D. Fernandez, R. C. Haskell, E. Huang, W. R. Myers,D. C. Petersen, S. E. Ungersma, R. Y. Wang, M. E. Williams, andS. E. Fraser, “An optical coherence microscope for 3-dimensional imaging in developmental biology,” Opt. Express, vol. 6, pp. 136–146, 2000.
4. E. Beaurepaire, A. C. Boccara, M. Lebec, L. Blanchot, and H. Saint-Jalmes, “Full-field optical coherence microscopy,” Opt. Lett., vol. 23, pp. 244–246, 1998.
5. M. Laubscher, M. Ducros, B. Karamata, T. Lasser, and R. Salathe ′ ,“Video-rate three-dimensional optical coherence tomography,” Opt. Express, vol. 10, pp. 429–435, 2002.
6. Woonggyu Jung, Jun Zhang, Lei Wang, Petra Wilder-Smith, Zhongping Chen, Member, IEEE, Daniel T. McCormick, and Norman C. Tien “Three-Dimensional Optical Coherence Tomography Employing a 2-Axis Microelectromechanical Scanning Mirror” IEEE JOURNAL OF SELECTED TOPICS IN QUANTUM ELECTRONICS, VOL. 11, NO. 4, JULY/AUGUST 2005
7. Anik Duttaroy, Andrew Paek Maristela Onozato, Bobak Shirmahamoodi James Jiang, Alex Cable, Peter M. Andrews, Yu Chen, “High-resolution Optical Coherence Tomography (OCT) Imaging of Human Kidney Ex Vivo”
8. Compact Ultrafast Reflective Fabry-Pérot Tunable Lasers For OCT Imaging Applications”, Mark Kuznetsov*, Walid Atia, Bart Johnson, and Dale Flanders. Optical Coherence Tomography and Coherence Domain Optical Methods in Biomedicine XIV. Edited by Izatt, Joseph

A.; Fujimoto, James G.; Tuchin, Valery V. Proceedings of the SPIE, Volume 7554, pp. 75541F-75541F-6 (2010).

9. SPIE_BiOS2010_Compact Ultrafast Reflective Fabry-Pérot Tunable Lasers 20100126_presentation, Mark Kuznetsov*, Walid Atia, Bart Johnson, and Dale Flanders Axsun Technologies Inc., 1 Fortune Dr, Billerica, MA 01821, USA
10. D. C. Flanders, “Tunable Fabry-Pérot filter,” US Patent 6,373,632, issued April 16, 2002.
11. Nguyen, F.T.; Zysk, A.M.; Chaney, E.J.; Adie, S.G.; KotynekJ.G.; Oliphant, U.J.; Bellafiore, F.J.; Rowland, K.M.; Johnson, P.A.; Boppart, S.A.; “Optical Coherence Tomography: The Intraoperative Assessment of Lymph Nodes in Breast Cancer” Engineering in Medicine and Biology Magazine, IEEE Issue Date: March-April 2010 Volume: 29 Issue:2 page(s): 63 – 70
12. Purnima D. L. Greenwood, David T. D. Childs, Kenneth Kennedy, Kristian M. Groom, Maxime Hugues, Mark Hopkinson, Richard A. Hogg, Nikola Krstaji´c, Louise E. Smith, Stephen J. Matcher, Marco Bonesi, Sheila MacNeil, and Rod Smallwood “Quantum Dot Superluminescent Diodes for Optical Coherence Tomography: Device Engineering”, IEEE JOURNAL OF SELECTED TOPICS IN QUANTUM ELECTRONICS, VOL. 16, NO. 4, JULY/AUGUST 2010
13. Branislav Grajciar, Oldrich Ondracek , “FULL FIELD FOURIER DOMAIN OPTICAL COHERENCE TOMOGRAPHY”, Applied Electronics 2006,Pilsen 6-7 September 2006
14. M. A. Choma, M. V. Sarunic, C. Yang, and J. A. Izatt, “Sensitivity advantage of swept source and Fourier domain optical coherence tomography,” Opt. Express, vol. 11, pp. 2183–2189, 2003.
15. S. H. Yun, G. J. Terarney, J. F. de Boer, and B. E. Bouma, “Pulsed-source and swept-source spectral-domain optical coherence tomography with reduced motion artifacts,” Opt. Express, vol. 12, pp. 5614–5624, 2004.

16. R. Huber, M. Wojtkowski, K. Taira, J. G. Fujimoto, and K. Hsu, “Amplified, frequency swept laser for frequency domain reflectometry and OCT imaging: Design and scaling principles,” Opt. Express, vol. 13, pp. 3513–3528, 2005.
17. Y. Yasuno, V. D. Madjarova, S. Makita, M. Akiba, A. Tmrosawa, C.Chong, T. Sakai, K. Chan, M. Itoh, and T. Yatagai, “Three-dimensional and high-speed swept-source optical coherence tomography for in vivo investigation of human anterior eye segments,” Opt. Express, vol. 13, pp. 10652–10664, 2005.
18. R. Huber, M. Wojtkowski, J. G. Fujimoto, J. Y. Jiang, and A. E. Cable, “ Three-dimensional and C-mode OCT imaging with a compact, frequency swept laser source at 1300 nm,” Opt. Express, vol. 13, pp. 10523–10538, 2005.
19. Sang-Won Lee, Chang-Seok Kim, and Beop-Min Kim “External Line-Cavity Wavelength-Swept Source at 850 nm for Optical Coherence Tomography,” IEEE PHOTONICS TECHNOLOGY LETTERS, VOL. 19, NO. 3, FEBRUARY 1, 2007
20. A. Bilenca, S. H. Yun, G. J. Tearney, and B. E. Bouma, “Numerical study of wavelength-swept semiconductor ring lasers: the role of refractive index nonlinearities in semiconductor optical amplifiers and implications for biomedical imaging applications,” OPTICS LETTERS / Vol. 31, No. 6 / March 15, 2006,pp 760-762
21. S. H. Yun, C. Boudoux, M. C. Boudoux, J. F. de Boer, G. J. Tearney, and B. E. Bouma, IEEE Photonics Technol. Lett. 16, 293 (2004).
22. D. C. Flanders, W. A. Atia, B. C. Johnson, M. E. Kuznetsov, C. R. Melendez, “Optical coherence tomography laser with integrated clock,” US Patent Application 2009/0290167 A1
23. E. A. Avrutin, V.V. Nikolaev, and D.Gallagher, “Monolithic mode-locked semiconductor lasers”, in: J.Piprek (Ed.), *Optoelectronic Devices - Advanced Simulation and Analysis, Springer, NY, 2005, pp. 185-215*
24. Markus-Christian Amann, Jens Buus, “Tunable Laser Diodes”, Norwood, MA 02062, 1998, pp 33-35.

25. Karthik Kumar, Jonathan C. Condit, Austin McElroy, Nate J. Kemp, Kazunori Hoshino, Thomas E. Milner, and Xiaojing Zhang, “Forward-Imaging Swept Source Optical Coherence Tomography using Silicon MEMS Scanner for High-Speed 3-D Volumetric Imaging”, Optical MEMS and Nanophotonics, 2007 IEEE, MA4, pp10-11
26. A. P. Bogatov, P. G. Eliseev, and B. N. Sverdlov, Anomalous interaction of spectral modes in a semiconductor laser, IEEE J. Quantum Electron., 1975, V. **11**, No. 7, pp. 510-515
27. 1 . L.A.Coldren and S.W. Corzine, Diode Lasers and Photonic Integrated Circuits (Wiley, New York, 1995)
28. Avrutin E A, Marsh J H, and Portnoi E L, “Monolithic and multi-GigaHertz mode-locked semiconductor lasers: Constructions, experiments, models and applications”, IEE Proc. Optoelectronics, **147**, No 4, 251-278**,** Aug 2000

9 Appendices

List of variables and values

Active layer thickness (cm), d	0.03d-4
Auger recombination coefficient, C	1d-29
Gain compression factor, ε	1d-17
Non-radiative recombination time, τ_{nr}	10d-9
Optical confinement factor	0.02
Refractive index, n	3.5
Spontaneous emission factor	0.3d-5
Transparency carrier density, N_0	1.7d18

This paper appears in: Numerical Simulation of Optoelectronic Devices (NUSOD), 2011 11th International Conference on
Issue Date: 5-8 Sept. 2011
On page(s): 141 - 142
Location: Rome
ISSN: 2158-3234
Print ISBN: 978-1-61284-876-1
INSPEC Accession Number: 12304492
Digital Object Identifier: 10.1109/NUSOD.2011.6041182
Date of Current Version: 10 October 2011

[http://ieeexplore.ieee.org/xpls/abs_all.jsp?arnumber=6041182&tag=1]